

Linear analysis characterizes pressure gradient history effects in turbulent boundary layers

Salvador R. Gomez^{1,†} and Beverley J. McKeon¹

¹Center for Turbulence Research, Stanford University, Stanford, CA 94305, USA

(Received 5 August 2024; revised 9 October 2024; accepted 16 November 2024)

Adverse pressure gradient (APG) turbulent boundary layers (TBL) require an understanding of the details of the pressure gradient, or history effect, to characterize the associated variation of spatiotemporal turbulent statistics. The streamwise-varying mean pressure gradient is reflected in the streamwise developing mean flow field and thus resolvent analysis, which captures the amplification of the Navier–Stokes equations linearized about the turbulent mean, can be used to understand linear amplification in APG TBLs. In particular, by using a biglobal approach in which the amplification is characterized by a temporal frequency and spanwise wavenumber, the streamwise and wall-normal inhomogeneities of the APG TBL can be resolved and related to the APG history. The linear response is able to identify multiscale phenomena, identifying a near-wall peak with $\lambda_z^+ \approx 100$ for zero pressure gradient TBLs and mild to moderate APG TBLs as well as large-scale modes whose amplification increases with APG strength and Reynolds number. It is shown that the monotonic growth in the turbulent statistics with increasing APG is reflected in the linear growth in the associated resolvent amplification. Collapse in the Reynolds stresses is obtained through an augmented hybrid velocity scale, which replaces the local APG strength measure in the hybrid velocity scale presented in Romero *et al.* (*Intl J. Heat Fluid Flow*, vol. 93, 2022, 108885) with a velocity that encapsulates the pressure gradient history. While this resolvent approach is applicable to any APG TBL, it is shown from a scaling analysis of the linearized Navier–Stokes equations that the linear growth observed in the resolvent amplification with the history effect is limited to near-equilibrium APG TBLs.

Key words: boundary layer structure, turbulent boundary layers, turbulence theory

† Email address for correspondence: gomezsr@stanford.edu

© The Author(s), 2025. Published by Cambridge University Press. This is an Open Access article, distributed under the terms of the Creative Commons Attribution licence (<http://creativecommons.org/licenses/by/4.0>), which permits unrestricted re-use, distribution and reproduction, provided the original article is properly cited.

1. Introduction

Adverse pressure gradients (APGs) arise in many industrial applications, such as the flow over an airplane wing or within a diffuser. To isolate the effect of the APG from the surface curvature, many studies focus on the flat plate turbulent boundary layers (TBL) with an applied APG. In an experiment, the APG can be created by a converging/diverging ceiling (Volino 2020), an obstacle in the free stream (Vishwanathan *et al.* 2021) or wall-normal transpiration (Clauser 1954; Marusic & Perry 1995) to decelerate the free stream velocity while in simulations, the free stream velocity is prescribed through a boundary condition (Kitsios *et al.* 2016; Bobke *et al.* 2017; Lee 2017). Whereas the statistics of the canonical zero pressure gradient (ZPG) TBL are parameterized solely by its local Reynolds number, Re , the APG TBL statistics are parameterized by the local Re , a measure of the local pressure gradient strength, and a measure of the upstream pressure gradient conditions or history effect (Schlatter & Örlü 2010; Monty, Harun & Marusic 2011; Bobke *et al.* 2017; Vinuesa *et al.* 2017). A characterization of the history effect on the turbulent statistics remains difficult because measurements and analysis of the upstream, streamwise variation of the flow field is required.

The friction Reynolds number, Re_τ , the local ratio of the outer boundary layer thickness, δ_{99} , to the viscous length scale, ℓ_ν , is often used as the Reynolds number to parameterize wall-bounded turbulent flows, like a channel or a TBL. There have been various scaling relationships presented to collapse different regions of the mean turbulent flow for different Re_τ including the near-wall, log-region and wake regions (Coles 1956; Pope 2000; Wei *et al.* 2005; Marusic *et al.* 2013). While both the outer-scaled wake structures and intermediate large-scale structures in the log region, such as the attached eddies or very large-scale motions, become increasingly energized with Re_τ , the effect is most evident in the latter as a secondary peak in the log region emerges at sufficiently high Re_τ (Smits, McKeon & Marusic 2011; Lee & Moser 2015; Deshpande *et al.* 2023). This intensifies the Reynolds stresses in viscous units throughout the boundary layer, primarily in the outer region of the flow, for both ZPG and APG TBLs (Aubertine & Eaton 2005; Hutchins *et al.* 2009).

One measure of the APG strength in attached APG TBLs is the Clauser parameter (Clauser 1954), $\beta = (\delta^*/\tau_w)(dP/dx)$, where δ^* is the displacement thickness, τ_w is the wall-shear stress, P is the free stream pressure and x is the streamwise coordinate. This study will focus on mild to moderate APG with $\beta \leq 5$ such that the flow remains attached. An increase in β affects the APG TBL by increasing the wake in the mean velocity profile (Aubertine & Eaton 2005; Monty *et al.* 2011), energizing the large-scale structures that scale with δ_{99} in the wake region (Harun *et al.* 2013; Lee 2017; Sanmiguel Vila *et al.* 2020; Pozuelo *et al.* 2022) and a subsequent intensification of the Reynolds stresses in viscous units in both the inner and outer regions of the flow (Sanmiguel Vila *et al.* 2020). The energization of large-scales in the outer region creates secondary peaks in the turbulent fluctuations, even at low Re_τ (Bobke *et al.* 2017; Lee 2017), though these energized motions are primarily the outer-scaled structures in the wake rather than log region structures as evidenced in high Re_τ studies (Sanmiguel Vila *et al.* 2020; Deshpande *et al.* 2023). The differences in the APG TBL structure have inspired a variety of scaling relationships that collapse the turbulent statistics (Gungor *et al.* 2016; Sekimoto *et al.* 2019; Romero *et al.* 2022; Wei & Knopp 2023). While there are differences between APG and ZPG TBLs, primarily in the outer region of the TBL, the near-wall structure remains mostly unchanged (Harun *et al.* 2013; Bobke *et al.* 2017; Pozuelo *et al.* 2022). The premultiplied streamwise kinetic energy spectra in experiments and simulations identify a self-similar near-wall peak at $y = 15\ell_\nu$, $\lambda_x = 1000\ell_\nu$ and $\lambda_z = 100\ell_\nu$ for canonical

wall-bounded turbulent flows (Hoyas & Jiménez 2006; Marusic, Mathis & Hutchins 2010; Smits *et al.* 2011; Eitel-Amor, Örlü & Schlatter 2014; Lee & Moser 2015; Baidya *et al.* 2017) that are reflected in APG TBLs with similar length scales (Harun *et al.* 2013; Bobke *et al.* 2017; Lee 2017; Pozuelo *et al.* 2022; Deshpande *et al.* 2023).

Due to the history effect, which we will explore here in terms of the upstream variations in $\beta(x)$, the local parameters Re_τ and β are not able to fully parameterize the local turbulent statistics since the boundary layer adjusts from the upstream conditions over a finite distance. In order to characterize the history effect and its influence on the turbulent statistics, the analysis needs to account for the upstream variation in the flow. As the history effect influences the mean velocity field, it also affects quantities of engineering interest like the skin-friction. Vinuesa *et al.* (2017) proposed an empirical predictive skin-friction curve for APG TBLs based on ZPG TBL data by accounting for the history effect through an upstream average of β . Here, an upstream average of β will also be used as a measure for the history effect to quantify the accumulated β in the APG TBL at a given streamwise location. It has been shown that for two APG TBLs with locally matched Re_τ and β , the APG TBL with the larger accumulated β exhibits intensified streamwise fluctuations in the outer region and a stronger wake (Bobke *et al.* 2017; Tanarro, Vinuesa & Schlatter 2020).

Through the resolvent analysis framework of McKeon & Sharma (2010), the Fourier transformed velocity fluctuations are shown to be equal to the resolvent operator acting on the nonlinear terms in the Navier–Stokes equations (NSE). The resolvent operator is the inverse of the linearized NSE (LNSE) and captures the scale-dependent linear amplification from the mean flow field. In resolvent analysis, the resolvent operator is decomposed into an orthonormal forcing basis, ϕ_i , an orthonormal response basis, ψ_i , and linear gains σ_i . Due to the non-normality of the LNSE, the leading modes take advantage of the increased pseudoresonant amplification such that the leading forcing and response modes exploit sources of non-normal amplification in the TBL (Trefethen 1999; Schmid & Henningson 2002; Symon *et al.* 2018). For wall-bounded turbulent flows, the main sources of non-normality come from the componentwise non-normality from the mean shear responsible for the lift-up mechanism and Orr-like tilting (Jovanović & Bamieh 2005; Hwang & Cossu 2010). Linear analyses that take advantage of these non-normal mechanisms have been shown to identify two distinct spectral peaks when the LNSE is augmented with an eddy viscosity (Del Alamo & Jimenez 2006; Cossu, Pujals & Depardon 2009). For streamwise developing flow fields, the convective non-normality is also present. It has been shown that modes that take advantage of the lift-up mechanism from the componentwise non-normality lead to low-rank behaviour in the resolvent operator. For these modes, ψ_1 agrees well with the data-driven modes (Abreu *et al.* 2020, 2021) and the σ_i identify length scales akin to the near-wall cycle (Moarref *et al.* 2013). The convective non-normality manifests itself as upstream forcing that leads to downstream responses (Chomaz 2005; Sipp & Marquet 2013; Schmidt *et al.* 2018; Symon *et al.* 2018; Pickering *et al.* 2021). The convective and componentwise non-normalities are present in the biglobal resolvent approach, which has been applied to, for example, ZPG boundary layers (Sipp & Marquet 2013; Abreu *et al.* 2021), supersonic boundary layers (Kamal *et al.* 2020) and spatially developing jets (Jeun, Nichols & Jovanović 2016; Schmidt *et al.* 2018). The linear biglobal studies of Ran *et al.* (2019) on stochastic receptivity in a laminar boundary layer and Davis, Uzun & Alvi (2019) on streamwise energy growth in a ZPG TBL also take advantage of the non-normal mechanisms discussed herein.

While the resolvent framework gives accurate predictions for systems with uncorrelated white-noise forcing, turbulent flows have correlated and structured nonlinear forcing that can limit comparisons between the resolvent modes and turbulent statistics (Towne, Schmidt & Colonius 2018; Morra *et al.* 2021). This study focuses solely on the linear

amplification mechanisms in APG TBLs that amplify the nonlinear terms in the NSE while drawing similarities to the turbulent statistics. Here, biglobal resolvent analysis is used to include the non-parallel effects of the APG TBL encoded within the mean flow field. This includes the history effect, which will be shown to affect the linear amplification and can be characterized through a scaling analysis of the LNSE.

This paper is organized as follows. Section 2 will describe the resolvent analysis framework, details about the discretization and a description of the datasets used in this study. Section 3 focuses on the local β and Re_τ effects on the optimal response, $\sigma_1 \psi_1$, on both the small and large scales in low-moderate Re_τ TBLs. Section 4 demonstrates that the resolvent amplification, σ_i , of large-scale structures grows monotonically with a measure of the history effect. This linear monotonic growth with the history effect is then used to augment the hybrid velocity scale which improves the collapse of the Reynolds stresses (Sekimoto *et al.* 2019; Romero *et al.* 2022). An explanation for the linear growth is provided in § 5 through a simplified Orr–Sommerfeld–Squire (OSS) operator. A discussion of results is provided in § 6. Conclusions are presented in § 7.

2. Methodology

In this section, the biglobal resolvent approach is discussed for an incompressible TBL. This includes a description of the LNSE, the resolvent analysis framework, details of the numerical analysis and a description of the mean flow fields used herein.

2.1. Linearized Navier–Stokes equations

A statistically stationary incompressible TBL develops over a flat plate with a specified free stream velocity, $U_\infty(x)$. The streamwise, wall-normal and spanwise coordinates are x , y and z with $y = 0$ denoting the location of the wall and z assumed to be statistically homogeneous. The streamwise, wall-normal and spanwise velocities are u , v and w and the pressure divided by density is p . The domain is taken as a subset of the flat plate such that $x \in [x_i, x_o]$, where the leading edge and virtual origin of the TBL are both outside of the domain and $y \in [0, y_{max}]$, where y_{max} is in the free stream. Within the domain, reference locations, x_r , are used to define the length and velocity scales that non-dimensionalize the equations. Variables without superscripts are non-dimensionalized with the reference free stream velocity, $U_r = U_\infty(x_r)$, and the reference length scale, $\delta_{99,r} = \delta_{99}(x_r)$, where δ_{99} denotes the boundary layer thickness. Variables with + superscripts are non-dimensionalized with the reference friction velocity $u_{\tau,r} = u_\tau(x_r)$ and reference viscous length scale $\ell_v = \nu/u_{\tau,r}$, where $u_\tau = \sqrt{\tau_w/\rho}$. These reference length and velocity scales are then used to define the local outer Reynolds number, $Re = U_r \delta_{99,r}/\nu$ and local friction Reynolds number, $Re_\tau = u_{\tau,r} \delta_{99,r}/\nu$.

The instantaneous flow field, $\check{q}(x, t) = [\check{u}, \check{p}]^T$, can be written as the sum of a known mean flow field, $\bar{Q}(x, y) = [\bar{U}(x, y), \bar{P}(x, y)]^T$, and a fluctuation, $q(x, t) = [u(x, t), p(x, t)]^T$. For the boundary layer, $\bar{U} = \bar{U}(x, y)e_x + \bar{V}(x, y)e_y$. Due to the spanwise homogeneity and statistical stationarity of the flow, the NSE may be Fourier transformed in z and t . The Fourier transformed variables are denoted by $\hat{\cdot}$, such that

$$\hat{g}(x, y; k_z, \omega) = \int_t \int_z g(x, y, z, t) e^{i(\omega t - k_z z)} dz dt, \quad (2.1)$$

where $k_z = 2\pi/\lambda_z$ and $\omega = 2\pi/\lambda_t$ are the spanwise wavenumber and temporal frequency. λ_z and λ_t then denote the spanwise and temporal wavelengths. The equations governing

the Fourier modes with $(\omega, k_z) \neq (0, 0)$ are then

$$\begin{bmatrix} -i\omega + \bar{\mathbf{U}} \cdot \nabla + \nabla \bar{\mathbf{U}} - Re^{-1} \nabla^2 + \epsilon_s & \nabla \\ \nabla \cdot & 0 \end{bmatrix} \hat{\mathbf{q}} = \begin{bmatrix} -\nabla \cdot \widehat{\mathbf{u}} \\ 0 \end{bmatrix}, \quad (2.2)$$

where $\nabla = [\partial_x, \partial_y, ik_z]$, $\nabla^2 = \partial_{xx} + \partial_{yy} - k_z^2$ and ϵ_s is the sponge used for artificial boundary conditions. Following McKeon & Sharma (2010), the nonlinear terms in (2.2) are treated as a nonlinear forcing with spanwise wavenumber k_z and temporal frequency ω , $\hat{\mathbf{f}} = [\hat{\mathbf{f}}_u, 0]^T$. To focus on what insight can be obtained from the linear resolvent operator, the forcing is assumed to be uncorrelated from the turbulent fluctuations. While eddy viscosity can be used to incorporate turbulent interactions into the LNSE (Del Alamo & Jimenez 2006; Cossu *et al.* 2009; Hwang & Cossu 2010), their specific forms are data-driven or *ad hoc* and can obfuscate the true linear amplification in the NSE and the interpretability of the nonlinearities (Morra *et al.* 2021; Pickering *et al.* 2021). In this approach, $\hat{\mathbf{f}}$ can be interpreted as an externally applied body force.

No-slip and no-penetration boundary conditions are applied such that $\hat{\mathbf{u}}(x, y = 0) = \mathbf{0}$ is enforced. In the free stream, Neumann boundary conditions are applied such that $\partial_y \hat{\mathbf{u}}(x, y = y_{max}) = \mathbf{0}$. Since the streamwise domain is a subset of the flat plate with $x \in [x_i, x_o]$, artificial boundary conditions are applied in the streamwise direction such that $\hat{\mathbf{q}}$ remains compact within the domain. This is enforced through the sponge, $\epsilon_s(x)$, in (2.2), which is 0 for 90 % of the domain and ramps up quadratically from 0 to ϵ_0 at the endpoints of the domain. The explicit form of $\epsilon_s(x)$ is

$$\epsilon_s(x) = \begin{cases} \epsilon_0 \frac{(|x - x_c - L/2| - 0.45L_x)^2}{0.0025L^2} & \text{if } |x - x_c - L/2| \geq 0.45L, \\ 0 & \text{otherwise,} \end{cases} \quad (2.3)$$

where $L = x_o - x_i$ and x_c is the centre of the domain. ϵ_s causes $\hat{\mathbf{q}}$ to decay to $\mathbf{0}$ in the vicinity of the boundaries. Similar strategies have been applied for linear analyses of incompressible flows in Ran *et al.* (2019) and Abreu *et al.* (2021). The inlet and outlet of the domains are then treated with Dirichlet boundary conditions such that $\hat{\mathbf{q}}(x = x_i, y) = \hat{\mathbf{q}}(x = x_o, y) = \mathbf{0}$ to enforce the compact nature of the resolvent modes. The effect of the sponge is qualitatively similar to fringe zones that are commonly used in TBL simulations to dampen the outflow and allow for the treatment of periodic boundary conditions (Chevalier *et al.* 2007). In the calculations presented herein, $\epsilon_s = 30$. Varying this value was found to have a negligible effect on the linear amplification, provided that ϵ_s was large enough to dampen $\hat{\mathbf{q}}$ at the boundaries.

2.2. Resolvent analysis

Equation (2.2) can be written compactly as

$$(-i\omega \mathcal{B} + \mathcal{L})\hat{\mathbf{q}} = \mathcal{B}\hat{\mathbf{f}}, \quad (2.4)$$

where \mathcal{B} projects away the p component as $\mathcal{B}\hat{\mathbf{q}} = [\hat{\mathbf{u}}, 0]^T$. The kinetic energy of the disturbances, integrated over the domain, is a norm induced by the inner product,

$$\langle \mathbf{a}, \mathbf{b} \rangle = \frac{1}{L} \int_{x_i}^{x_o} \int_0^{y_{max}} \mathbf{a}^* \mathcal{B} \mathbf{b} \, dy \, dx. \quad (2.5)$$

By using this inner product, the adjoint of (2.2) can also be written compactly as

$$(i\omega \mathcal{B} + \mathcal{L}^\dagger)\tilde{\mathbf{q}} = \mathcal{B}\tilde{\mathbf{f}}, \quad (2.6)$$

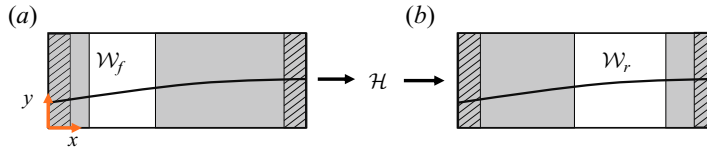


Figure 1. Schematic depicting in white the integration domains for $\|\cdot\|_f$ (a) and $\|\cdot\|_r$ (b). The striped regions at the edges of the domain depict the sponge layers and the black solid curve depicts a representative boundary layer edge.

where the daggers denote adjoint operators and tildes denote adjoint variables. An explicit form of the adjoint operator can be found in Gomez (2024). It is assumed that ω is not an eigenvalue of \mathcal{L} so that the resolvent, $\mathcal{H} = (-i\omega\mathcal{B} + \mathcal{L})^{-1}\mathcal{B}$, and adjoint resolvent, $\mathcal{H}^\dagger = (i\omega\mathcal{B} + \mathcal{L}^\dagger)^{-1}\mathcal{B}$, exist.

In resolvent analysis, one is interested in finding the forcing inputs of \mathcal{H} that lead to the largest amplification. Here, the forcing inputs and response outputs of \mathcal{H} are measured with the induced norms $\|\cdot\|_f$ and $\|\cdot\|_r$ from the inner products $\langle \mathbf{a}, \mathbf{b} \rangle_f = \langle \mathbf{a}, \mathcal{W}_f \mathbf{b} \rangle$ and $\langle \mathbf{a}, \mathbf{b} \rangle_r = \langle \mathbf{a}, \mathcal{W}_r \mathbf{b} \rangle$, respectively. Here, \mathcal{W}_r and \mathcal{W}_f are positive definite operators that dictate the components and spatial domains of $\hat{\mathbf{q}}$ and $\hat{\mathbf{f}}$ that are used to measure the response and the forcing. The exact form of \mathcal{W}_r and \mathcal{W}_f will be specified for the studies considered. An example of the regions included in the norms $\|\cdot\|_f$ and $\|\cdot\|_r$ are depicted in figure 1.

The linear amplification, σ , of \mathcal{H} is here defined as the Rayleigh quotient,

$$\sigma^2 = \frac{\|\mathcal{H}\hat{\mathbf{f}}\|_r}{\|\hat{\mathbf{f}}\|_f} = \frac{\langle \mathcal{H}\hat{\mathbf{f}}, \mathcal{W}_r \mathcal{H}\hat{\mathbf{f}} \rangle}{\langle \hat{\mathbf{f}}, \mathcal{W}_f \hat{\mathbf{f}} \rangle} = \frac{\langle \hat{\mathbf{f}}, \mathcal{H}^\dagger \mathcal{W}_r \mathcal{H} \hat{\mathbf{f}} \rangle}{\langle \hat{\mathbf{f}}, \mathcal{W}_f \hat{\mathbf{f}} \rangle}. \quad (2.7)$$

To find the largest amplification, one seeks the forcing, ϕ , that produces the largest σ such that

$$\phi = \underset{\|\hat{\mathbf{f}}\|_f=1}{\operatorname{argmax}} \sigma. \quad (2.8)$$

It can be shown that (2.8) can be solved via the eigenvalue problem,

$$\mathcal{H}\mathcal{W}_r\mathcal{H}^\dagger\phi_j = \sigma_j^2\mathcal{W}_f\phi_j. \quad (2.9)$$

Since $\mathcal{H}\mathcal{W}_r\mathcal{H}^\dagger$ and \mathcal{W}_f are positive definite operators, the eigenvalues, σ_j^2 , are positive and the eigenvectors, ϕ_j , are orthonormal with respect to the inner product $\langle \cdot, \cdot \rangle_f$ such that $\langle \phi_j, \phi_k \rangle_f = \delta_{jk}$, where δ_{jk} is the Kronecker delta. The σ_j are ordered such that $\sigma_1 \geq \sigma_2 \geq \dots \geq 0$. ϕ_j are here identified as the forcing modes with corresponding linear gain, σ_j . The response modes, ψ_j , are defined as $\psi_j = \sigma_j^{-1}\mathcal{H}\phi_j$. It can be shown that the response modes are orthonormal with respect to the inner product $\langle \cdot, \cdot \rangle_r$ such that $\langle \psi_j, \psi_k \rangle_r = \delta_{jk}$.

In this study, two sets of norms are considered. The first set is tailored to study the effect of local Re_τ and β on the linear amplification in § 3. This requires that the response modes are supported at x_{r1} where $\beta(x_{r1})$ and $Re_\tau(x_{r1})$ are defined. If there is no spatial masking applied to the inner product such that $\langle \cdot, \cdot \rangle_r = \langle \cdot, \cdot \rangle_f = \langle \cdot, \cdot \rangle$, then the response and forcing modes can be supported anywhere along the streamwise domain. In order to capture the modes at x_{r1} , spatial masking is applied to the response

modes so that

$$\langle \mathbf{a}, \mathbf{b} \rangle_r = \frac{1}{L^+} \int_{x_{r_1}^+ - L_d^+/2}^{x_{r_1}^+ + L_d^+/2} \int_0^{y_{max}} \mathbf{a}^* \mathcal{B} \mathbf{b} \, dy \, dx^+, \quad (2.10)$$

where $L_d^+ = 2150$, while $\langle \cdot, \cdot \rangle_f = \langle \cdot, \cdot \rangle$. The forcing modes can extend across the entire domain allowing forcing from upstream the spatial mask to influence the linear response within the spatial mask. This helps capture non-local amplification mechanisms like those from the convective non-normality. Here L_d is held constant in viscous units since the small-scale modes are expected to scale in inner units. For a mode to be optimal under the new inner products via the definition in (2.7), the optimal response modes must be supported in the streamwise region within $L_d^+/2$ of x_{r_1} . The effect of L_d^+ has been shown in the appendix of Gomez (2024), where it is shown that increasing L_d^+ reduces the response of the near-wall small-scale modes at x_{r_1} . The second set of inner products is used to study the history effects in § 4. In order to only consider the effect of the pressure gradient upstream of x_{r_2} , the inner products $\langle \cdot, \cdot \rangle_r$ and $\langle \cdot, \cdot \rangle_f$ are masked such that

$$\langle \mathbf{a}, \mathbf{b} \rangle_r = \langle \mathbf{a}, \mathbf{b} \rangle_f = \frac{1}{L_x} \int_{x_i}^{x_{r_2}} \int_0^{y_{max}} \mathbf{a}^* \mathcal{B} \mathbf{b} \, dy \, dx, \quad (2.11)$$

where x_i is 12 $\delta_{99}(x_{r_2})$ upstream of x_{r_2} . This makes the resolvent modes optimal in the sense of (2.8) if they are supported upstream of x_{r_2} and also prevents the amplification mechanisms present downstream of x_{r_2} from contributing to the linear amplification.

It is important to note that $\boldsymbol{\psi}_j$, $\boldsymbol{\phi}_j$ and σ_j are dependent on the (λ_z, λ_t) pair, \bar{U} , and choice of norms. Here $\boldsymbol{\psi}_j$ can be used to reconstruct the flow field as $\hat{\mathbf{q}} = \sum_j \xi_j \sigma_j \boldsymbol{\psi}_j$, where ξ_j are coefficients that are found through fitting to data or appealing to the full NSE. The studies herein will primarily consider the optimal response, $\sigma_1 \boldsymbol{\psi}_1$, as a rank-one approximation for the Fourier modes without any nonlinear closure. By taking an integral over ω , one can also define the premultiplied amplification,

$$\hat{E}(y^+; k_z^+) = k_z^+ \int_{\omega_{min}^+}^{\omega_{max}^+} |\sigma_1^+(k_z^+, \omega^+) \boldsymbol{\psi}_{u,1}^+(x_{r_1}^+, y^+; k_z^+, \omega^+)|^2 \, d\omega^+. \quad (2.12)$$

Here \hat{E} can be thought of as the premultiplied streamwise kinetic energy spectrum for a velocity signal under the rank-one representation, $\hat{\mathbf{u}} = \sigma_1 \boldsymbol{\psi}_{u,1}$. Here, $\hat{E}(y^+; k_z^+)$ is a measure of the linear amplification across all scales.

2.3. Numerical discretization

The domain is discretized with N_x equispaced points in the streamwise direction and N_y points in the wall-normal direction. The wall-normal grid points are stretched such that half the points are below y_{min} . Each wall-normal grid point, y_k , is mapped from an equispaced grid point, y'_k using $y_k = ay'_k / (b - y'_k)$ where $a = y_{max} y_{min} / (y_{max} - 2y_{min})$ and $b = 1 + a/y_{max}$. This is similar to the grids used in the supersonic linear analyses of Kamal *et al.* (2020) and Malik (1990), except here, the grid stretching is used to increase the resolution in the near-wall region of the TBLs studied. Both streamwise and wall-normal directions use a fourth-order summation by parts scheme for the differentiation operators (Mattsson & Nordström 2004). Once discretized, the operators \mathcal{B} , \mathcal{L} , \mathcal{L}^\dagger , \mathcal{H} and \mathcal{H}^\dagger become the $4N_x N_y \times 4N_x N_y$ matrices \mathbf{B} , \mathbf{L} , \mathbf{L}^\dagger , \mathbf{H} and \mathbf{H}^\dagger .

In order to perform the integration in (2.5), the streamwise and wall-normal integration is performed with a trapezoidal scheme. The positive definite matrix, \mathbf{W}_T , performs the integration in (2.5) such that

$$\langle \mathbf{a}, \mathbf{b} \rangle \approx \mathbf{a}^* \mathbf{W}_T \mathbf{b}. \quad (2.13)$$

In a similar fashion, the operators \mathcal{W}_r and \mathcal{W}_f are discretized with the diagonal matrices \mathbf{M}_r and \mathbf{M}_f . The diagonal entries of \mathbf{M}_r and \mathbf{M}_f are 0 for the entries omitted and 1 for the entries included in the inner products. As a result, the inner products for the discretized space are defined as

$$\langle \mathbf{a}, \mathbf{b} \rangle_r = \mathbf{a}^* \mathbf{M}_r \mathbf{W}_T \mathbf{b} = \mathbf{a}^* \mathbf{W}_r \mathbf{b}, \quad (2.14)$$

and

$$\langle \mathbf{a}, \mathbf{b} \rangle_f = \mathbf{a}^* \mathbf{M}_f \mathbf{W}_T \mathbf{b} = \mathbf{a}^* \mathbf{W}_f \mathbf{b}. \quad (2.15)$$

In the discretized space, the eigenvalue problem in (2.9) becomes

$$\mathbf{H} \mathbf{W}_r \mathbf{H}^\dagger \phi_j = \sigma_j^2 \mathbf{W}_f \phi_j, \quad (2.16)$$

while $\psi_j = \sigma_j^{-1} \mathbf{H} \phi_j$. Equation (2.16) is solved using the Arnoldi algorithm (Saad 2011). The matrices \mathbf{B} , \mathbf{L} , \mathbf{L}^\dagger , \mathbf{W}_r and \mathbf{W}_f are sparse, while the resolvent matrices, \mathbf{H} and \mathbf{H}^\dagger , are dense matrices that are costly to compute. The Arnoldi approach requires repeated calculations of $\mathbf{v} = \mathbf{H}\mathbf{b}$, or equivalently solving $(-i\omega\mathbf{B} + \mathbf{L})\mathbf{v} = \mathbf{B}\mathbf{b}$, and similarly for the adjoint. Following the approach described in Sipp & Marquet (2013) and Schmidt *et al.* (2018), LU decompositions of $(-i\omega\mathbf{B} + \mathbf{L})$ and $(i\omega\mathbf{B} + \mathbf{L}^\dagger)$ are computed once. The LU factors can then efficiently solve $(-i\omega\mathbf{B} + \mathbf{L})\mathbf{v} = \mathbf{B}\mathbf{b}$ through Gaussian elimination. Thus, the overall cost of the Arnoldi algorithm is the cost of the LU decompositions (Jeun *et al.* 2016). The LU decomposition and Gaussian elimination is computed using the Intel oneAPI Math Kernel Library PARDISO (Schenk & Gärtner 2004), which is optimized for the sparse form of the matrices and uses parallelized subroutines. See the appendix of Gomez (2024) for an algorithm explaining this strategy in more detail.

2.4. Description of datasets

This study focuses on mild to moderate APG TBL where $\beta \in [0, 5]$. Since the large-scale modes require large streamwise domains to both be resolved and achieve significant amplification, only studies with large, well-resolved streamwise domains, relative to $\delta_{99}(x_r)$, are considered. The mean flow fields of interest are the large eddy simulation flat plate TBL data of Bobke *et al.* (2017), Pozuelo *et al.* (2022) and Eitel-Amor *et al.* (2014) which each have domains upstream of x_{r2} larger than $20\delta_{99}(x_{r2})$. The datasets all use a constant free stream velocity, $U_\infty(x)$, followed by an APG imposed by the boundary condition $U_\infty(x) = (x - x_0)^m$, where x_0 and m are specified to create varying degrees of APG strengths. Under this regime, the APG TBLs are in the ‘near-equilibrium’ regime (Mellor & Gibson 1966; Townsend 1976; Bobke *et al.* 2017).

A brief description of the parameters of interest in the datasets are described in table 1. In this study, the Clauser parameter is defined as

$$\beta(x) = \frac{\delta^*(x)}{u_\tau^2(x)} \frac{dP}{dx}(x, y = \delta_{99}(x)), \quad (2.17)$$

as in Bobke *et al.* (2017) and Pozuelo *et al.* (2022). Pozuelo *et al.* (2022) notes that the free stream boundary conditions in the simulations cause \bar{U} to decrease in the wall-normal

| Dataset | m | x_0/δ_0^* | Re_τ range | $\beta(x_{r_1})$ | $\beta(x_{r_2})$ | $\langle\beta_\infty\rangle$ | Colour |
|---------|-------|------------------|-----------------|------------------|------------------|------------------------------|--------|
| S0 | 0 | 0 | (190, 2569) | 0 | 0 | 0 | — |
| b1 | -0.14 | 110 | (190, 862) | 1.00 | 0.78 | 0.90 | — |
| m13 | -0.13 | 60 | (190, 896) | — | 0.91 | 1.04 | — |
| b14 | -0.16 | 60 | (190, 2256) | — | 1.65 | 1.48 | — |
| b2 | -0.18 | 110 | (190, 910) | 2.10 | 1.56 | 1.95 | — |
| m16 | -0.16 | 60 | (190, 934) | — | 1.66 | 2.19 | — |
| m18 | -0.18 | 60 | (192, 973) | 4.37 | 2.09 | 3.48 | — |

Table 1. Parameters describing the datasets, along with quantities of interest. The parameters m and x_0 set the PG in each simulation. Note that the Re_τ range is listed for the entire dataset, although only subsets of the domains are considered in this study. The streamwise locations x_{r_1} and x_{r_2} are chosen such that $Re_\tau(x_{r_1}) = 550$ and $Re_\tau(x_{r_2}) = 777$. Here $\langle\beta_\infty\rangle$ is computed following (2.19). The ZPG dataset, S0, is from Eitel-Amor *et al.* (2014) and the APG dataset, b14, is from Pozuelo *et al.* (2022) while the rest are from Bobke *et al.* (2017).

location from its peak at the boundary layer edge such that dP/dx at $y = \delta_{99}$ is different from the imposed pressure gradient (PG) through the free stream boundary condition. Due to this, the parameter

$$\beta_\infty(x) = \frac{\delta^*(x)}{u_\tau^2(x)} \frac{dP}{dx}(x, y_{max}) = \frac{\delta^*(x)}{u_\tau^2(x)} \frac{dP_\infty}{dx}(x), \tag{2.18}$$

will also be used to account for the effect of the free stream boundary condition. Here, β_∞ is used to parameterize the effect of history by accounting for the streamwise variation of the imposed APG boundary condition. In this study, the history effect is quantified by

$$\begin{aligned} \langle\beta_\infty\rangle &= \frac{1}{x_{r_2} - x_{i,2}} \int_{x_{i,2}}^{x_{r_2}} \beta_\infty(x) dx \\ &= \frac{1}{x_{r_2} - x_{i,2}} \int_{x_{i,2}}^{x_{r_2}} \int_0^\infty \frac{1}{u_\tau^2(x)} (1 - \bar{U}(x, y)) \frac{dP_\infty}{dx}(x) dy dx, \end{aligned} \tag{2.19}$$

where $x_{i,2}$ is an upstream location. Here, $x_{i,2} = x_{r_2} - 12\delta_{99}(x_{r_2})$ corresponds to the inlet location of the domains used to study the history effect in § 4. Here $\langle\beta_\infty\rangle$ is similar to the streamwise average that Vinuesa *et al.* (2017) considered, though they averaged β over the momentum thickness-based Reynolds number. The domains used in Vinuesa *et al.* (2017) for the averaging were $O(10\delta_{99})$ large, which is consistent with the averaging domain used here. Furthermore, (2.19) offers a measure of the APG history in a manner analogous to the streamwise averaging induced by the inner product in (2.11).

Figure 2(a) shows the variation of β with Re_τ for the datasets used, along with the values at the reference locations used in this study. Figure 2(b–d) show \bar{U}^+ , \overline{uu}^+ and \bar{V}^+ at fixed x_{r_2} . Consistent with the observations from previous studies described above, these mean flow fields demonstrate monotonic growth in the wake velocity and decreasing \bar{U}^+ in the log-layer region with increasing β . Monotonic growth in the secondary peak of \overline{uu}^+ is observed with $\langle\beta_\infty\rangle$, with the near-wall peak of \overline{uu}^+ also affected. The non-monotonic behaviour in \bar{V}^+ with $\langle\beta\rangle_\infty$ highlight the non-equilibrium nature of the datasets, with different levels of deceleration in the flow at x_{r_2}

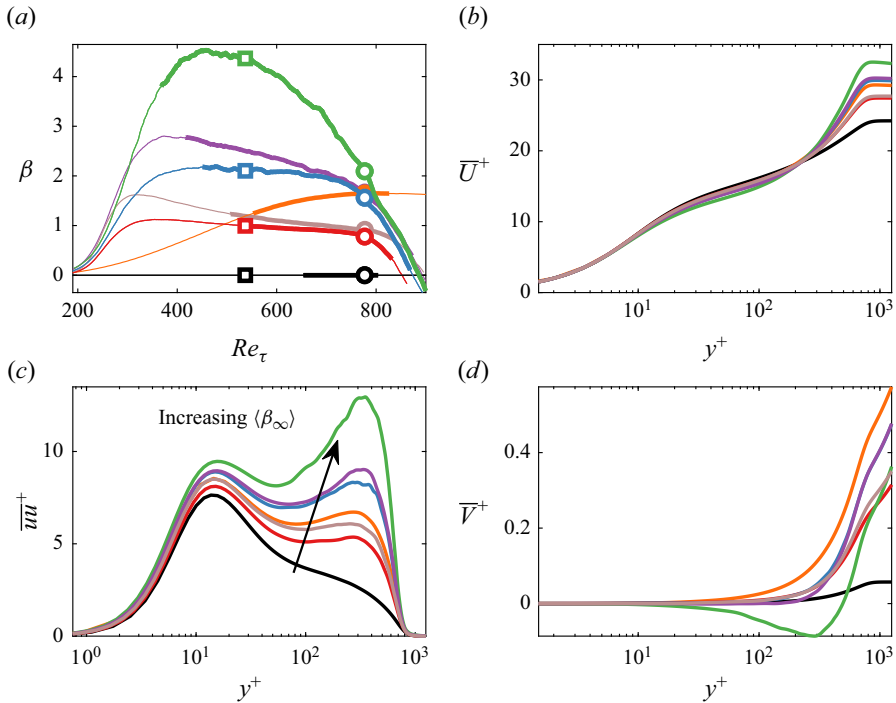


Figure 2. (a) Here β plotted against Re_τ for the APG datasets described in table 1. The solid lines indicate the domain used to study the history effect. The values evaluated at x_{r_2} and x_{r_1} are plotted with circles and squares, respectively. The thicker lines denote the subdomains used in § 4 to study the history effect. Plots of \bar{U}^+ (b), \overline{uu}^+ (c) and \bar{V}^+ (d) against y^+ at x_{r_2} . The viscous units are also computed at x_{r_2} .

| Case | Database | $Re_\tau(x_{r_1})$ | N_x | N_y | y_{max} | y_{min} |
|------|----------|--------------------|-------|-------|-----------|-----------|
| 1 | S0 | 537 | 900 | 251 | 5 | 0.24 |
| 2 | b1 | 537 | 900 | 251 | 5 | 0.24 |
| 3 | b2 | 537 | 900 | 251 | 5 | 0.24 |
| 4 | m18 | 505 | 750 | 251 | 5 | 0.23 |
| 5 | S0 | 1500 | 1100 | 251 | 3 | 0.14 |
| 6 | S0 | 1800 | 1200 | 251 | 3 | 0.13 |
| 7 | b14 | 1500 | 1100 | 251 | 3 | 0.14 |

Table 2. Local Re_τ and grid information for the different studies in § 3.

3. Effect of local parameters on linear amplification

In this section, the local effects of $\beta(x_r)$ and $Re_\tau(x_r)$ on the linear amplification are examined. Here, the reference viscous and outer length and velocity scales are defined at x_{r_1} . Table 2 describes quantities of interest used for the seven case studies in this section. In order to support the large-scale modes, the domains are set with $L_x = 43.44$, which corresponds to the entire domain of the b2 dataset, except for case 4 whose entire domain is $L_x = 36.6$ long. To resolve small-scale structures near the wall, $y_{min} = 0.24\sqrt{537/Re_\tau}$ in cases 5–7 so that y_{min} is proportional to the start of the log-layer (Wei *et al.* 2005). Since

δ_{99} does not grow as rapidly for larger Re_τ TBL, cases 5–7 reduce the y_{max} to 3 to further increase the resolution within the boundary layer while maintaining $y_{max} > \delta_{99}(x)$.

3.1. Effect of masking on the response and forcing modes

Here, the goal is to study the linear response of large- and small-scale modes subject to different local parameters. This requires that the response modes are supported at x_{r_1} where $\beta(x_{r_1})$ and $Re_\tau(x_{r_1})$ are defined. Without a spatial mask, the response and forcing modes can be supported anywhere along the streamwise domain. It was shown that the small-scale modes, characterized by $O(\lambda_z^+) \leq O(100)$, were amplified via the componentwise non-normality from the mean shear near the wall while the large-scale modes, characterized by $O(\lambda_z) \geq O(1)$, extended into the outer region of the flow and were amplified via the convective non-normality (Gomez 2024). As a result, the unmasked small-scales are expected to be concentrated in the upstream region where they experience the largest mean shear within the domain. The unmasked large-scale modes can extend across the entire domain, with the largest forcing amplitude concentrated upstream and the largest response amplitude concentrated downstream (Sipp & Marquet 2013; Symon *et al.* 2018).

As an example for how the leading resolvent modes behave without masking, ψ_1 and ϕ_1 are computed for a representative small-scale mode with $(\lambda_z^+, \lambda_t^+) = (50, 50)$ and a representative large-scale mode with $(\lambda_z, \lambda_t) = (1, 1.4)$ using case 3. In figure 3(a,b), $\phi_{v,1}$ and $\sigma_1 \psi_{u,1}$ are plotted for the representative small-scale and in figure 3(c,d) for the representative large-scale. As alluded to earlier, without masking, the small-scale modes are concentrated upstream of x_{r_1} while the large-scale mode is supported at x_{r_1} . For these unmasked modes, the amplitude of $\psi_1(y, x_{r_1})$ is negligible for the small-scale mode and serves as a poor measure of the linear response at x_{r_1} .

In figure 3(e,f), the modes from figure 3(a,b) are recomputed using the spatial masking described in (2.10). Both the representative small-scale $\phi_{v,1}$ and $\psi_{u,1}$ are supported at x_{r_1} with the spatial mask. Due to the larger Re_τ at x_{r_1} compared with the inlet location and fixed λ_z and λ_t across the domain in the calculation, the modes plotted in figure 3(e,f) have significantly smaller wall-normal extents and streamwise wavelengths than those in figure 3(a,b). This is because the small-scale modes are amplified by the large mean shear concentrated in the viscous subregion, whose wall-normal extent scales with ℓ_v . As Re_τ increases downstream, ℓ_v decreases and constrains the length scales of the modes. Now the representative large-scale modes from figure 3(c,d) are recomputed using the same spatial masking and plotted in figure 3(g,h). Since $\langle \cdot, \cdot \rangle_f$ is left unchanged, the modes can still be amplified via the convective non-normality. As a result, the large-scale forcing can still be supported upstream of x_{r_1} while its response is supported downstream of x_{r_1} . However, because of the spatial masking, the optimal forcing is primarily concentrated upstream of x_{r_1} since any forcing downstream of $x_{r_1} + L_d/2$ would lead to a response outside of the spatial mask without contributing to σ_1 . This also highlights the non-local nature in the amplification of large-scale structures and their susceptibility to upstream history effects that is explored in more detail in § 4.

For the rest of this section, the spatial masking described in (2.10) is applied to identify optimal small and large-scale responses at x_{r_1} .

3.2. Effect of β on linear amplification at low Re_τ

To investigate the effect of local $\beta(x_{r_1})$, cases 1–4 are examined since they have a similar $Re_\tau(x_{r_1})$ and different values of $\beta(x_{r_1})$. Furthermore, the slow variation in $\beta(x)$ near x_{r_1}

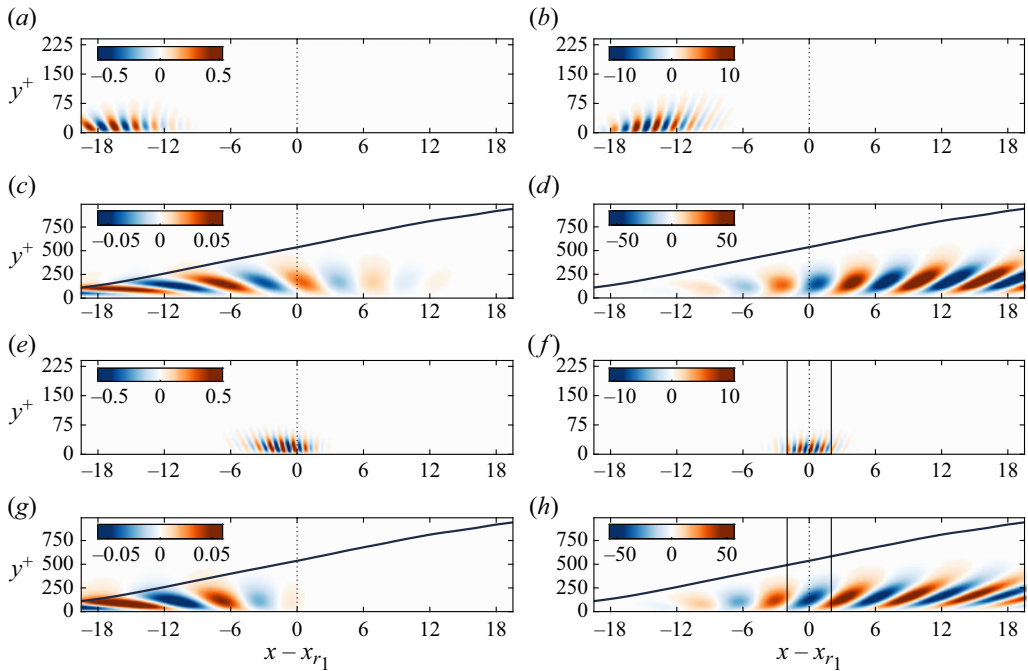


Figure 3. Real parts of $\phi_{v,1}$ (*a,c,e,g*) and $\sigma_1\psi_{u,1}$ (*b,d,f,h*) for the representative small-scale (*a,b,e,f*) and large-scale (*c,d,g,h*) modes using case 3. The modes in (*a-d*) are computed without masking in the inner product while the modes in (*e-h*) are computed using masking from (2.10) in the inner product for the response modes. The edges of the spatial mask are plotted with the black solid vertical lines. The dotted line is the reference location, x_{r_1} . The curved solid line denotes the local boundary layer thickness.

minimizes the influence of $d\beta/dx$ or history on the linear amplification between cases 1–4. Here, the effect of $\beta(x_{r_1})$ on the resolvent amplification is compared for a wide range of scales.

First, the streamwise component of the linear response of the ZPG TBL of case 1 and the APG TBL of case 3 are compared for a large-scale mode ($\lambda_t^+ = 200, \lambda_z = 1$) and small-scale mode ($\lambda_t^+ = 50, \lambda_z^+ = 50$) in figure 4. Plotted in figure 4(*a-c*), the effect of the APG on the large-scale response at x_{r_1} is an increase in the magnitude and peak amplitude location farther from the wall than the ZPG counterparts. Since these large-scale modes have support, i.e. non-negligible amplitude, in the outer region of the TBL, it is expected that they are most susceptible to the APG effects. On the other hand, the near-wall small-scale modes plotted in figure 4(*d-f*) are only slightly affected by the change in the mean flow field. This is because for this mild APG, the near-wall is still dominated by viscous effects and the APG hardly affects the inner scaling of \bar{U}^+ . These near-wall resolvent modes have been shown to be self-similar in the region where the mean flow field demonstrates self-similarity (Moarref *et al.* 2013; Gomez 2024).

While it is illustrative to compare the effect of β on individual modes, we now consider the effect of increasing β over a range of scales. The leading masked response modes are computed over a range of 31 logarithmically spaced k_z^+ between $2\pi/9.5$ and $2\pi/11\,000$ and 33 logarithmically spaced ω^+ between $2\pi/1.25$ and $2\pi/20\,000$. This range of k_z^+ and ω^+ is wide enough to capture the small-scale and large-scale modes and encompasses the characteristic length and time scales of the expected energy-containing structures in

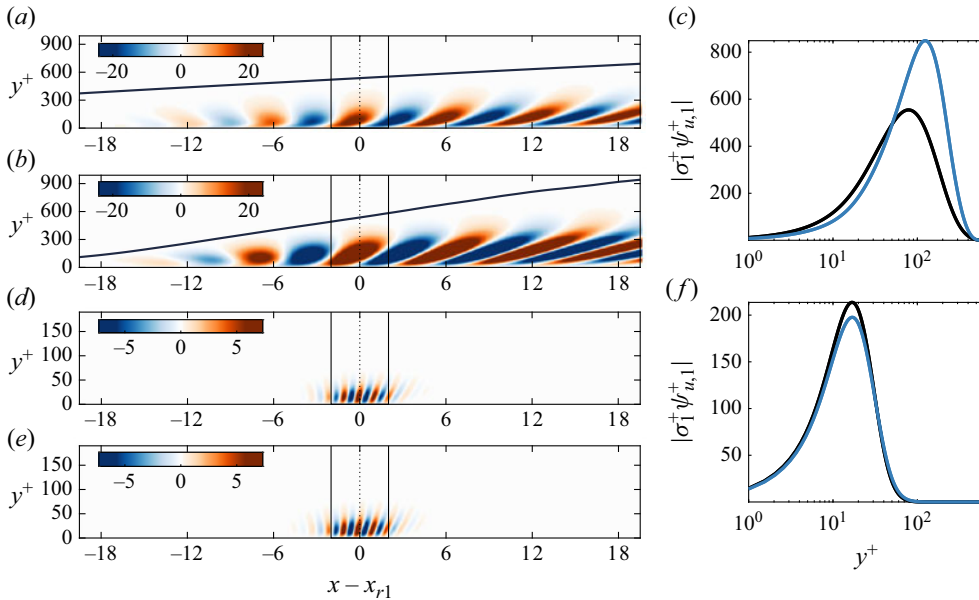


Figure 4. Real parts of $\sigma_1^+ \psi_{u,1}^+$ (*a,b,d,e*) for large-scale (*a,b*) and small-scale (*d,e*) modes using case 1 (*a,d*) and case 3 (*b,e*). The black lines are the same as those plotted in figure 3. Line plots of $|\sigma_1^+ \psi_{u,1}^+(y^+, x_{r1})|$ for the large-scale (*c*) and small-scale (*f*) modes. Black and blue denote modes computed using cases 1 and 3, respectively.

the actual TBLs. The premultiplied amplification spectra, $\hat{E}(y^+, k_z^+)$, (see (2.12)) are then computed for each β .

In figure 5, \hat{E}^+ is computed for cases 1–4. For the ZPG in case 1, \hat{E}^+ identifies only a near-wall peak with a local maximum near $y^+ = 20$ and $\lambda_z^+ = 77$. The lack of a secondary peak in the premultiplied amplification at this low Re_τ is similar to what is observed in the true premultiplied kinetic energy spectra for low Re_τ ZPG TBL and channels, which are dominated by the near-wall cycle. For the APG TBLs in cases 2–4, a near-wall peak is also observed. For case 2, this local maximum occurs at the same location as case 1, while for cases 3 and 4, the local maxima is at $y^+ = 20$ and $\lambda_z^+ = 60$.

Here \hat{E}^+ predicts higher wall-normal locations and smaller wavelengths for the near-wall peak than observed in the turbulent data of ZPG and mild to moderate APG TBLs. Besides the assumption of uncorrelated (uncoloured) forcing, one reason for this discrepancy is that in cases 1–4, δ_{99} varies substantially while λ_z remains fixed across the domain. As an example, in case 3, the $\lambda_z^+ = 100$ mode has a $\lambda_z = 0.19\delta_{99}(x_{r1}) = 1.20\delta_{99}(x_i)$. That is, near the inlet, the $\lambda_z^+ = 100$ mode is larger than the δ_{99} at the inlet. This in turn causes the $\lambda_z^+ = 100$ mode at x_{r1} to behave like a large-scale mode and experiences amplification via the convective non-normality, rather than the componentwise non-normality characteristic of the small-scale modes. As a result, the λ_z^+ modes are absent from the near-wall peak for these low Re_τ TBLs. The changing nature of the mode behaviour with streamwise distance is a challenge unique to the TBL relative to the canonical internal flows. It was shown in Gomez (2024) that by also applying masking to the forcing such that $\langle \cdot, \cdot \rangle_f = \langle \cdot, \cdot \rangle_r$, a local maximum could be found in \hat{E}^+ with $\lambda_z^+ \approx 100$ for both ZPG and APG TBLs.

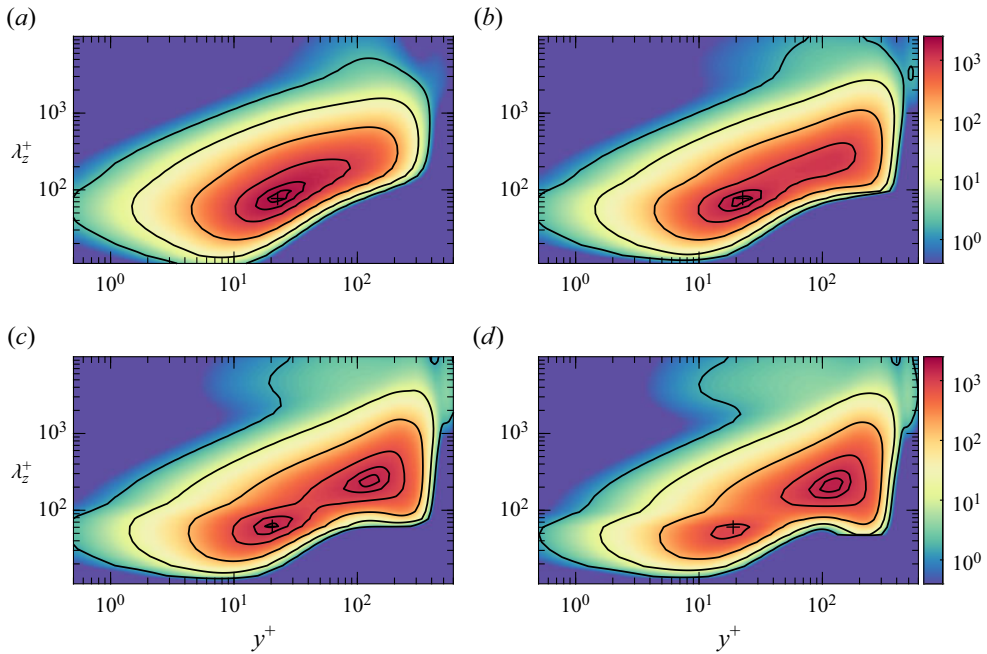


Figure 5. Here $\hat{E}^+(y^+; \lambda_z^+)$ is plotted against y^+ and λ_z^+ for case 1 (a), case 2 (b), case 3 (c) and case 4 (d); the value of $\beta(x_{r_1})$ increases monotonically from (a) to (d). The black contour lines in each subplot are spaced as 95 %, 82 %, 50 %, 10 %, 1 % and 0.1% of the maximum value of $\hat{E}^+(y^+; \lambda_z^+)$.

Despite the simplified forcing assumption, \hat{E}^+ also demonstrates a secondary peak for large-scale modes farther from the wall for the APG TBLs in cases 2–4. The secondary peak in \hat{E}^+ is amplified monotonically with increasing β . Similarly, a monotonic increase in the secondary peak of the spanwise kinetic energy spectra was observed in the DNS data of Lee (2017) at similar Re_τ to the mean data used here. For larger Re_τ , the streamwise energy spectra in the experiment also demonstrate large-scale secondary peaks that are energized with increasing β (Sanmiguel Vila *et al.* 2020). Despite the similar trends seen with β , there is again a discrepancy in the location of the secondary peaks in \hat{E}^+ and those of similar low Re_τ spanwise energy spectra (Bobke *et al.* 2017; Lee 2017). The secondary peaks in figure 5(b–d) occur at $\lambda_z^+ \approx 0.5Re_\tau$ whereas the turbulent data reports $\lambda_z^+ \approx 0.8Re_\tau - 0.9Re_\tau$. The discrepancy is likely attributable to the lack of nonlinear closure, but may again be in part related to the change in δ_{99} across the domain, as a mode of the order of $\delta_{99}(x_{r_1})$ at x_{r_1} would be around $6\delta_{99}(x_i)$ for case 3. Since the large-scale modes are forced from the upstream location, the smaller upstream boundary layer can affect the behaviour of the amplification at x_{r_1} by geometrically constraining the modes that can be amplified downstream. Nonetheless, the masked biglobal resolvent approach is able to capture the presence of both a small-scale, near-wall peak and a large-scale peak that is amplified monotonically with increasing β .

3.3. Effect of Re_τ on linear amplification

Linear amplification is now considered using the ZPG TBL dataset of Eitel-Amor *et al.* (2014) for the low Re_τ case 1 and larger Re_τ case 6. The large Re_τ APG TBL dataset of Pozuelo *et al.* (2022) (case 7) is also used to study the β effects in the linear amplification

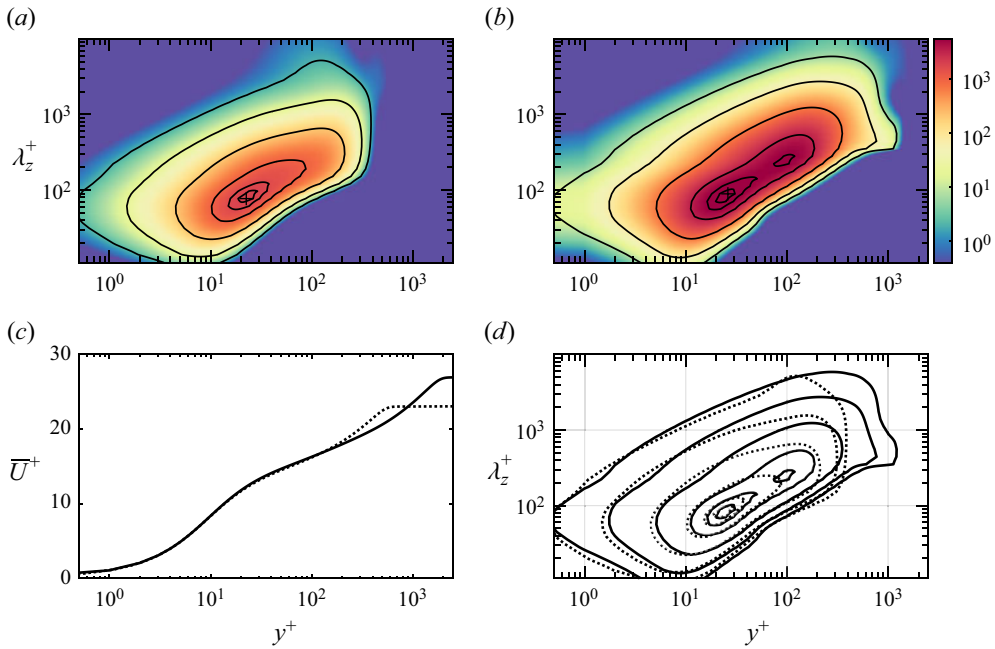


Figure 6. Here $\hat{E}^+(y^+, k_z^+)$ is plotted against y^+ and λ_z^+ for case 1 (a) and case 6 (b). Here $\bar{U}^+(x_{r1}, y^+)$ (c) and contour lines of $\hat{E}^+(y^+, k_z^+)$ (d) for cases 1 and 6 plotted in dotted and solid lines, respectively. The contours in (a), (b) and (d) denote 95 %, 82 %, 50 %, 10 %, 1 % and 0.1% of the maximum value of $\hat{E}_{uu}^+(y^+, \lambda_z^+)$.

at higher Re_τ by comparing with case 5 at the matched $Re_\tau = 1500$. The sweeps are computed using the same k_z and ω range as the previous results while the wall-normal stretching has been adjusted to resolve the smaller inner region in the larger Re_τ datasets by shrinking y_{min} .

Figure 6(a,b) show the variation of \hat{E}^+ for cases 1 and 6. Along with the near-wall peaks, \hat{E}^+ also demonstrate increased amplification for the large-scale modes with increasing Re_τ with case 6 showing evidence of a secondary peak. This secondary peak occurs at a wall-normal location slightly closer to the wall than the secondary peaks of the APG results in figure 5, potentially pointing to a difference between log and APG-amplified wake structures. However, the Re_τ is too small to adequately distinguish between the two. Figure 6(d) provides direct comparison of isocontours of \hat{E}^+ for cases 1 and 6. These plots demonstrate that \hat{E}^+ is self-similar in the near-wall region due to the inner-scaled mask in $(\cdot, \cdot)_r$ and self-similar mean flows, plotted in figure 6(c) for reference. The near-wall self-similarity of the resolvent amplification in individual modes had been studied for channel flows in Moarref *et al.* (2013) and spatially developing TBLs in Gomez (2024) where the response and forcing modes are spatially constrained via small, inner-scaled, streamwise domains. Figure 6(d) demonstrates that the self-similarity in the resolvent modes persists in \hat{E}^+ even when the forcing modes are not spatially constrained with a spatial mask or limited domain length. As the large-scale outer-scaled resolvent modes become more amplified farther from the wall, the near-wall self-similarity of \hat{E}^+ breaks because the inner-scaled self-similarity of \bar{U} no longer holds.

Now, the effect of β is considered for the large Re_τ APG TBL from case 7. These results are directly compared with those of case 5 which is at the same Re_τ , with their

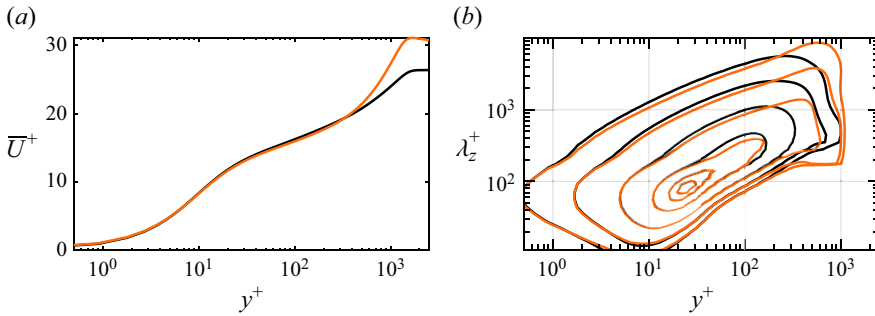


Figure 7. Here $\bar{U}^+(x_{r_1}, y^+)$ (a) and contour lines of $\hat{E}^+(y^+; k_z^+)$ (b) for cases 5 and 7 plotted in black and orange lines, respectively. The contours in (b) denote 95 %, 82 %, 50 %, 10 %, 1 % and 0.1 of the maximum value of $\hat{E}_{uu}^+(y^+; \lambda_z^+)$.

mean velocity profiles compared in figure 7(a). At this larger Re_τ and mild β , the inner region of the mean flow is hardly affected by the APG. As a result, \hat{E}^+ exhibits near-wall self-similarity in figure 7(b), like case 6. For \hat{E}^+ , the self-similarity breaks at larger λ_z^+ , indicating that these large-scale modes are more sensitive to the changes in the mean flow field than the near-wall small-scale modes. Just as was seen in figure 5, the large-scale modes are more amplified for the APG TBL than the ZPG TBL in the higher Re_τ case, similar to the energization of the outer-scaled spectral peak in the APG TBL observed in Pozuelo *et al.* (2022).

The masked biglobal resolvent analysis approach is able to capture Re_τ trends seen in the spanwise energy spectra. A self-similar near-wall peak and increased amplification in the large-scale structures with Re_τ are observed. At matched Re_τ , the linear amplification increases with β . For sufficiently large Re_τ , a secondary peak is also observed. Although this analysis is restricted to a rank-one approximation, it nonetheless suggests that changes in the linear amplification from a change in the mean flow field due to Re_τ and β can explain features seen in experimental and simulation data without any nonlinear closure in the form of a scale-dependent coefficient. It can thus be surmised that these are phenomena associated with the dominant behaviour of the linear resolvent whose predictions can be improved by more sophisticated modelling of the details of the nonlinear forcing.

4. History effect on the linear amplification of large-scale modes

It was noted in several studies, and plotted in figure 2(c), that an increase in the measure of the accumulated upstream pressure gradient strength results in an increase in the streamwise turbulent fluctuations (Bobke *et al.* 2017; Tanarro *et al.* 2020; Pozuelo *et al.* 2022). In this section, the effect of the upstream pressure gradient, or history effect, on the linear amplification is studied by using the biglobal resolvent analysis. Although the PG does not enter the LNSE, the history effect is manifested in the LNSE through the pressure gradient's effect on \bar{U} . The calculations in this section will use the datasets from table 1 with the numerical details described in table 3. From figure 2(a), it can be seen that all the datasets begin with different values of $\beta(x_i)$ while at x_{r_2} all the domains have matched $Re_\tau(x_{r_2})$ and some have similar $\beta(x_{r_2})$, like m16, b2 and b14. The rich β values allow for the study of history effects and allows for the comparison of cases where the local β and Re_τ are matched. Including the m18 dataset also allows for a study over a relatively large range of accumulated APG strength with $\beta_\infty \in [0.9, 3.5]$ and the ZPG dataset with

| N_x | L_x | $(x_i - x_{r_2})/L_x$ | N_y | y_{max} | y_{min} |
|-------|-------|-----------------------|-------|-----------|-----------|
| 450 | 15.89 | 0.765 | 251 | 5 | 0.226 |

Table 3. Numerical details for the calculations used in §4. The domains are streamwise sections of the datasets described in table 1 such that $x - x_{r_2} \in [-0.815, 0.185]L_x$ where $Re_\tau(x_{r_2}) = 777$. Values here non-dimensionalized with $\delta_{99}(x_{r_2})$.

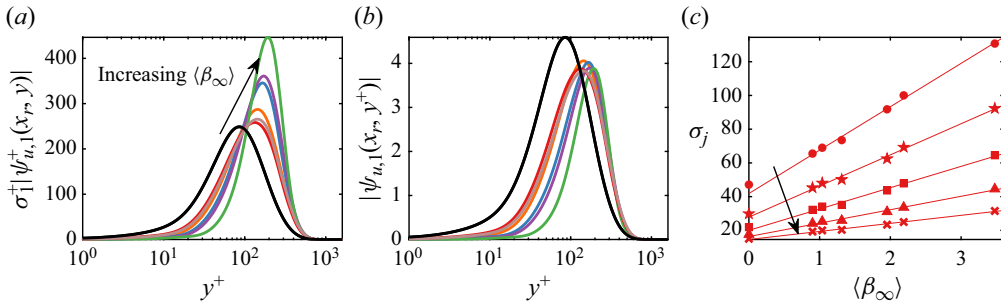


Figure 8. Response modes and resolvent amplification for a large-scale mode with $\lambda_z = 2, \lambda_t = 4.48$. $|\sigma_1^+ \psi_{u,1}^+(x_{r_2}, y^+)|$ (a) and $|\psi_{u,1}(x_{r_2}, y^+)| = \sqrt{Re_\tau(x_{r_2})} |\psi_{u,1}^+(x_{r_2}, y^+)|$ (b). The colours are colour coded according to table 1 and the arrow in (a) denotes increasing $\langle \beta_\infty \rangle$. $\sigma_j = \sigma_j^+ Re / Re_\tau^2$ for the same large-scale mode, with the arrow denoting the direction of increasing j . $j = 1, 2, 3, 4$ and 5 correspond to the circle, star, square, triangle and \times . The lines are lines of best fit, fitted for $\langle \beta_\infty \rangle > 0$.

$\langle \beta_\infty \rangle = 0$. Here, the modes are computed using the masking described in (2.11) and the parameters described in table 3. Additionally, $L_x = 15.89$ to avoid the low Re_τ region in the database where β ramps up quickly as seen in figure 2(a), particularly for the m18 dataset. Because the APG effects are present mostly in the outer region of the TBL, this section will focus on the history effect on the large-scale modes, like those plotted in figure 4(a–c), since they extend into the outer region of the flow.

In §5, quantities are normalized with the length and velocity scales at x_{r_2} and the inner products in (2.11) are used. Biglobal resolvent analysis is computed for a representative large-scale, $\lambda_z = 2, \lambda_t = 4.48$. Figure 8(a) demonstrates a monotonic increase in $|\sigma_1^+ \psi_{u,1}^+(x_{r_2}, y^+)|$ with $\langle \beta_\infty \rangle$, similar to the monotonic growth in \overline{uu}^+ with $\langle \beta_\infty \rangle$ in figure 2(c). Here, cases b14 and m16 are specifically highlighted since their $\beta(x_{r_2}) \approx 1.65$ and $Re_\tau(x_{r_2}) = 777$ while $\langle \beta_\infty \rangle$ differ by approximately 48%. The variation in their linear responses, $|\sigma_1^+ \psi_{u,1}^+(x_{r_2}, y^+)|$, evidences non-negligible sensitivity to the upstream flow conditions. This is unsurprising given the convective non-normality that amplifies these large-scale modes through upstream forcing present in this biglobal approach. It is also worth noting that the ZPG mean flow field produces a mode that peaks closer to the wall than the modes computed with the APG TBL mean flow fields. This may point to an amplification mechanism for the log-layer structures in the ZPG TBL while the APG TBL amplifies modes in the wake. However, studies with sufficiently high Re_τ with adequate scale separation would be needed to adequately disambiguate between the log and wake region structures. Nonetheless, the differences in the ZPG and APG response modes are likely due to the significantly different \bar{U} in the ZPG TBL that produces a wake that does not follow the outer scaling for APG TBL studied in Wei & Knopp (2023) as well as the negligible wall-normal convection from \bar{V} in the ZPG TBL.

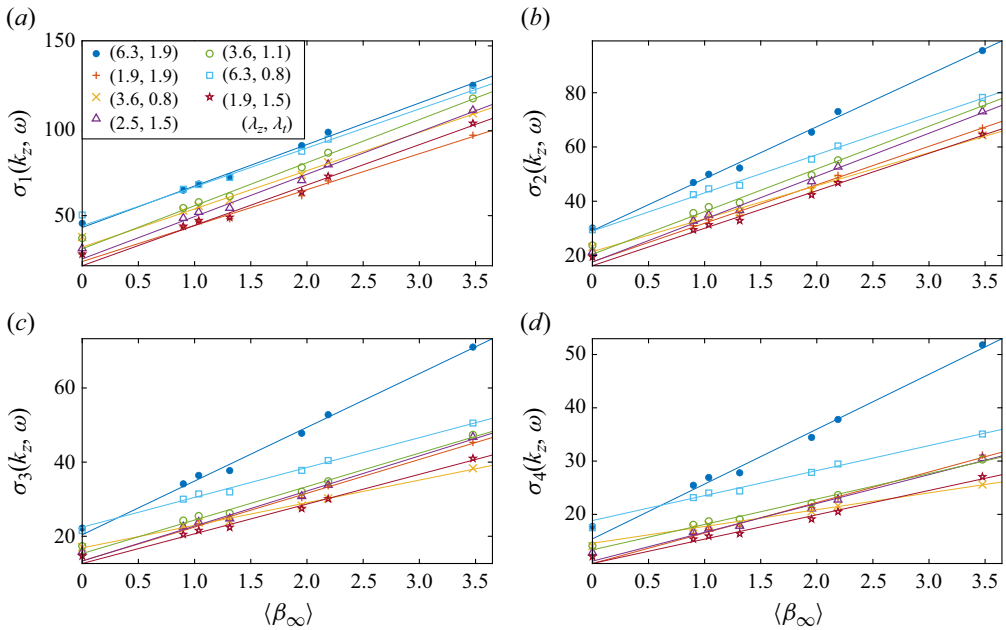


Figure 9. Plots of σ_1 (a), σ_2 (b), σ_3 (c) and σ_4 (d) against $\langle \beta_\infty \rangle$ computed with the λ_z and λ_t from the legend in (a). The solid lines denote the lines of best fit, fitted for $\langle \beta_\infty \rangle > 0$.

To show that the increase in $|\sigma_1^+ \psi_{u,1}^+|$ is due to the change in σ , figure 8(b) plots $|\psi_{u,1}|$, demonstrating that for the APG TBL modes, the mode shape amplitude is approximately $\langle \beta_\infty \rangle$ independent. The modes with increased $\langle \beta_\infty \rangle$ are farther from the wall due to the increased wall-normal advection throughout the domain. Figure 8(c) plots σ_j for $j = 1, 2, 3, 4, 5$. Here σ_j grows approximately linearly with $\langle \beta \rangle$ for $\langle \beta_\infty \rangle > 0$, as evidenced by the lines of best fit. The σ_j for $\langle \beta_\infty \rangle = 0$ do not fall on the line, likely because of the difference in the outer region of \bar{U} that also causes $\psi_{u,1}$ to peak closer to the wall. The effects of the wall-normal advection and non-parallel shear terms absent in the ZPG TBL will be expanded upon later in § 5.

In figure 9, σ_j for $j = 1, 2, 3, 4$ is plotted against $\langle \beta_\infty \rangle$ for a variety of λ_z and λ_t , characteristic of large-scale structures. Just like in figure 8(b), the σ_j grows approximately linearly with $\langle \beta_\infty \rangle$ such that for $\langle \beta_\infty \rangle > 0$,

$$\sigma_j(\lambda_z, \lambda_t) \approx m_{j,0}(\lambda_z, \lambda_t)[1 + m_{j,1}(\lambda_t, \lambda_z)\langle \beta_\infty \rangle], \quad (4.1)$$

where $m_{j,0}$ and $m_{j,1}$ are λ_z and λ_t dependent positive constants for each gain, σ_j . Once again, the σ_j computed with the ZPG TBL \bar{U} do not fall on this linear fit. Equation (4.1) encapsulates the influence of the history effect on the linear amplification through a streamwise averaged measure of β . As mentioned before, similar streamwise averaged measures of β have been proposed before to account for the history effect in turbulent statistics (Vinuesa *et al.* 2017) and the effect of an increased accumulated pressure gradient has been shown to intensify the streamwise fluctuations (Tanarro *et al.* 2020). Here, the history effect is shown to produce a monotonic increase in the linear amplification.

Now we study if the monotonic growth in \overline{uu}^+ with $\langle \beta_\infty \rangle$ is reflected in the linear growth of σ_1 with $\langle \beta_\infty \rangle$. The hybrid velocity scale, u_h , studied in Romero *et al.* (2022) and Sekimoto *et al.* (2019) showed that by rescaling the Reynolds stresses with u_h^2 , the APG induced outer peaks are mitigated. Here u_h augments u_τ with a wall-normally varying

pressure velocity, $u_p^2(y) = ydp/dx = \beta u_\tau^2 y/\delta^*$, as

$$u_h^2(y) = u_\tau^2 + u_p^2(y) = u_\tau^2 \left(1 + \frac{y}{\delta^*} \beta\right). \quad (4.2)$$

Notably, u_h^2/u_τ^2 demonstrates linear growth with β , if the effect of β on δ^* is neglected. However, u_h is not explicitly parameterized by any terms related to the history effect as it constructed from local mean flow quantities. Through the observation of linear growth of σ_1 with $\langle\beta_\infty\rangle$, an augmented hybrid velocity scale is proposed as

$$u_{hyb}^2(y) = u_\tau^2 + \frac{\langle\beta_\infty\rangle}{\beta} u_p^2(y) = u_\tau^2 \left(1 + \frac{y}{\delta^*} \langle\beta_\infty\rangle\right), \quad (4.3)$$

which simply replaces β in (4.2) with $\langle\beta_\infty\rangle$. This form of u_{hyb} is inspired through two assumptions in mild to moderate APG TBLs. The first is that the characteristic velocity scale close to the wall is u_τ , regardless of β or $\langle\beta_\infty\rangle$. The second is that u_{hyb}^2 has an explicit linear dependence on $\langle\beta_\infty\rangle$ like σ_j in (4.1) because of the increased linear amplification of large-scale turbulent structures present in the outer region of the TBL. The velocity scale accounts for history effects by increasing the role of u_p if $\langle\beta_\infty\rangle > \beta$ and decreasing its influence otherwise.

In figure 10(b), \overline{uu} is normalized with u_h^2 as in Romero *et al.* (2022) and Sekimoto *et al.* (2019) demonstrating that it can remove the secondary peaks in \overline{uu} . However, because u_h is a local measure, it cannot account for the monotonic growth in \overline{uu}^+ with $\langle\beta_\infty\rangle$. This is reflected with the b14 (orange) falling below the curves of b2 (blue) and m16 (purple) in the outer region despite their similar values of $\beta(x_{r_2})$. Furthermore, m18 (green) falls above the other curves because of its larger upstream β values. Figure 10(c) demonstrates improved collapse across the entire boundary layer compared with \overline{uu}/u_h^2 by accounting for history effects. In a similar sense, figure 10(d–i) demonstrate that while rescaling \overline{uv} and \overline{vv} with u_h^2 mitigates the $\langle\beta_\infty\rangle$ intensified outer region turbulent fluctuations, using u_{hyb}^2 improves the collapse of the Reynolds stresses by accounting for the larger β_∞ effects upstream. This serves to show that a linear dependence in $\langle\beta_\infty\rangle$ is reflected in the APG turbulent statistics of Bobke *et al.* (2017) and Pozuelo *et al.* (2022), not just the linear amplification of their mean flow fields. Furthermore, it suggests that a characterization of the turbulent statistics requires knowledge of the pressure gradient history.

Extending this velocity scale to other datasets requires a measurement of $\beta(x)$ over a long upstream region of the flow to compute the streamwise averages, which is often not reported. For the calculation of $\langle\beta_\infty\rangle$ used in u_{hyb} , this study averaged β_∞ over a streamwise domain of $12\delta_{99}$ upstream of x_{r_2} , which coincides with the domain of integration used in the inner product in (2.11) that quantifies the linear amplification. Since, u_{hyb} is based on an analogy with (4.1), which is obtained by the linear amplification in ‘near-equilibrium’ APG TBLs (Bobke *et al.* 2017), we caution that the scaling of the Reynolds stresses is not a general result for APG TBLs. As explained in more detail in the following section, the linear scaling on σ_j is not guaranteed to hold for general non-equilibrium APG TBLs.

5. Explanation of the linear $\langle\beta_\infty\rangle$ dependence on the amplification

Here, it will be shown that the linear relationship between σ_j and $\langle\beta_\infty\rangle$ can be predicted from the LNSE. In order to do so, several simplifying assumptions are made. First, it is assumed that the modes computed using the APG TBLs are independent of the mean flow field based on the observation from figure 8(b). Because of this, only the APG TBL modes

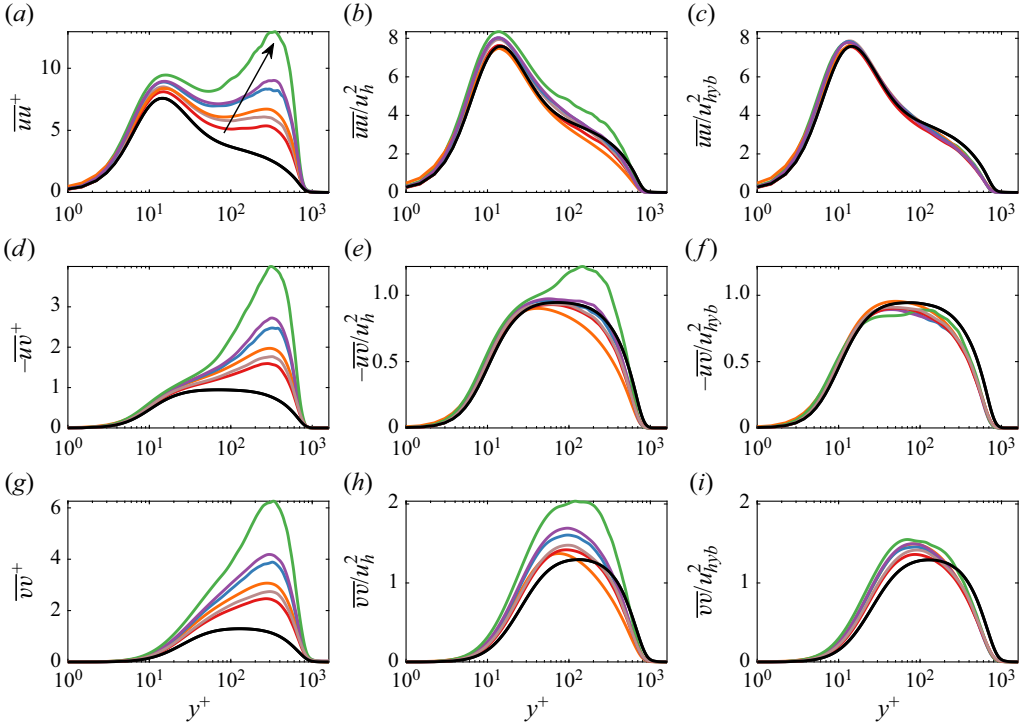


Figure 10. Plots of \overline{uu} (a–c), $-\overline{uv}$ (d–f) and \overline{vv} (g–i) at x_{r_2} . (a,d,g) are normalized with u_τ^2 , (b,e,h) are normalized with u_h^2 and (c,f,i) are normalized with u_{hyb} . The line colours are labelled in table 1. Note that (a) is replotted from figure 2(c). The arrow denotes increasing $\langle \beta_\infty \rangle$.

will be considered since the ZPG TBL modes have significantly different behaviour since the outer region of the ZPG TBL has a different structure from the APG TBL (Wei & Knopp 2023). Second, the dominant terms in the LNSE are determined by comparing the advection ($\bar{U}\partial_x$, $\bar{V}\partial_y$) and mean shear (\bar{U}_y , \bar{U}_x , \bar{V}_x) terms. Specifically, the terms are compared in the outer region by using the norm

$$\|f\|_o^2 = \frac{1}{L_x} \int_{x_i}^{x_{r_2}} \int_{y_o}^{y_{max}} |f|^2 dy dx, \quad (5.1)$$

where $y_o^+ = 40$ since the modes of interest are large-scale modes supported in the outer region of the flow as plotted in figure 8(a). This also enables the assumption that $\|\partial_x \psi_{i,j}\|_o \sim O(\delta_{99}^{-1} \|\psi_{i,j}\|_o)$, $\|\partial_y \psi_{i,j}\|_o \sim O(\delta_{99}^{-1} \|\psi_{i,j}\|_o)$ and $k_z \sim O(\delta_{99}^{-1})$ since the length scales of the large-scale modes scale with the outer length scale. Note that due to the non-dimensionalization with the outer units, $\delta_{99} \sim O(1)$. As a result, the measure of the advection terms is approximated as $\|\bar{U}\partial_x\| \sim O(\|\bar{U}\|_o)$ and $\|\bar{V}\partial_y\| \sim O(\|\bar{V}\|_o)$.

In figure 11, the shear and advection terms are compared using the norm in (5.1). Due to the increasing APG, the non-parallel terms increase in magnitude with $\langle \beta_\infty \rangle$. Here $\|\bar{U}\|_o$ increases monotonically with $\langle \beta_\infty \rangle$ because the norm is a measure of \bar{U} upstream of x_{r_2} . Due to the streamwise deceleration in APG flows, the stronger APG have larger upstream \bar{U} relative to x_{r_2} . Because of the increased boundary layer growth in APG flows, δ_{99} is significantly smaller upstream relative to $\delta_{99}(x_{r_2})$. These two effects create stronger upstream \bar{U}_y with increasing $\langle \beta_\infty \rangle$. For the datasets studied here, $\|\bar{U}_y\|_o$ grows linearly with $\langle \beta_\infty \rangle$, as shown in figure 11(d). As one may expect from the typical boundary layer

Linear analysis characterizes pressure

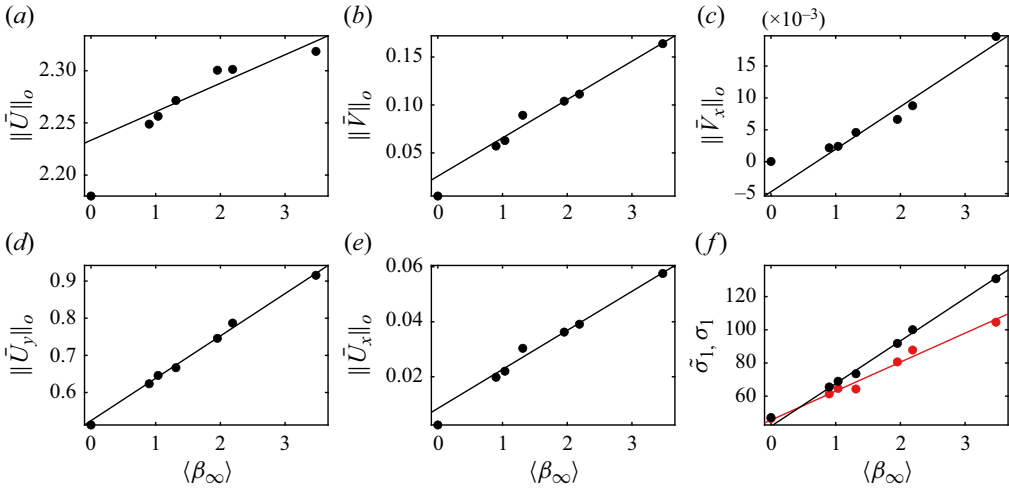


Figure 11. Plots of $\|\bar{U}\|_o$ (a), $\|\bar{U}\|_o$ (b), $\|\bar{V}_x\|_o$ (c), $\|\bar{U}_y\|_o$ (d) and $\|\bar{U}_x\|_o$ (e) against $\langle \beta_\infty \rangle$ as black filled circles. Finally, (f) plots $\tilde{\sigma}_1$, the leading singular values from the large-scale modes plotted in figure 8 recomputed with the non-parallel terms \bar{U}_x , \bar{V}_x and \bar{V} artificially set to 0 in the biglobal resolvent operator (black circles). For reference, the singular values from the full system, σ_1 are plotted in open blue circles. In each plot, the red lines denote lines of best fit for $\langle \beta_\infty \rangle > 0$. The lines in (f) denotes the lines of best fit for $\langle \beta_\infty \rangle > 0$ for σ_1 (black) and $\tilde{\sigma}_1$ (red).

assumptions (Pope 2000), the streamwise advection is an order of magnitude larger than the wall-normal advection while \bar{U}_y is at least an order of magnitude larger than \bar{U}_x and \bar{V}_x for the APG TBL datasets used herein.

To see if the non-parallel terms \bar{V} , \bar{U}_x and \bar{V}_x are responsible for the linear growth of σ_j with $\langle \beta_\infty \rangle$, the non-parallel terms are artificially set to 0 in the LNSE. Although the streamwise derivatives are not explicitly included in the LNSE, \bar{U} and \bar{U}_y are allowed to vary in x for this analysis. In figure 11(f), this assumption is tested for the same modes plotted in figure 8(a) by computing $\tilde{\sigma}_1$, the leading singular values of the biglobal resolvent operator with the non-parallel terms set to 0. By neglecting the non-parallel terms, the linear growth with $\langle \beta_\infty \rangle$ is still observed in $\tilde{\sigma}_1$. The non-parallel terms are a non-negligible source of amplification for the linear operator as the difference between σ_1 and $\tilde{\sigma}_1$ increases with $\langle \beta_\infty \rangle$. However, their omission in the analysis can still be used to explain the growth with $\langle \beta_\infty \rangle$. As a consequence, an additional assumption is that the non-parallel terms can be neglected in the explanation of the linear growth of σ_1 with $\langle \beta_\infty \rangle$.

In this section, the linear growth of σ_1 with $\langle \beta_\infty \rangle$ is first investigated using the assumption that the non-parallel terms can be neglected. Then the effects of the non-parallel terms on the linear amplification will be discussed. Finally, the section concludes with implications of this analysis for more general APG TBLs.

5.1. Neglecting the non-parallel terms to explain the linear growth

By neglecting \bar{V} , \bar{V}_x and \bar{U}_x , the LNSE in (2.2) can be approximated using the simplified forced biglobal OSS system,

$$\hat{v} = \mathcal{L}_{OS}^{-1} \hat{f}_v, \quad (5.2)$$

$$\hat{\omega}_2 = \mathcal{L}_{SQ}^{-1} (\hat{f}_\omega + ik_z \bar{U}_y \mathcal{L}_{OS}^{-1} \hat{f}_v), \quad (5.3)$$

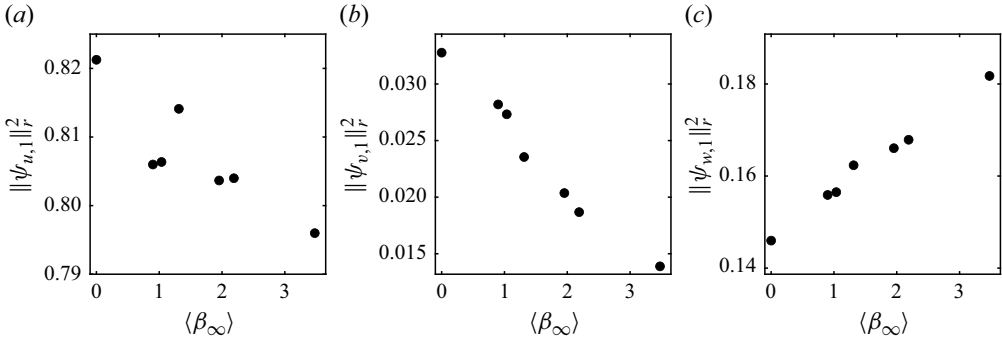


Figure 12. Plots of each of the terms in $\|\psi_1\|_r^2$ for the representative mode from figure 8.

where $\mathcal{L}_{SQ} = -i\omega + \bar{U}\partial_x - Re^{-1}\nabla^2$, $\mathcal{L}_{OS} = (-i\omega + \bar{U}\partial_x - (1/Re)\nabla^2) - 2\nabla^{-2}\partial_y(\bar{U}_y\partial_x)$, $\hat{f}_\omega = ik_z\hat{f}_x - \partial_x\hat{f}_z$ and $\hat{\omega}_2 = ik_z\hat{u} - \partial_x\hat{w}$. See the Appendix for more details. The resolvent gains of this system will then be denoted as $\tilde{\sigma}_j$. The forced biglobal OSS system has been studied by Ran *et al.* (2019) to identify the stochastic receptivity of a laminar boundary layer using the LNSE. In that case, terms involving \bar{U}_{xx} and \bar{V}_x were neglected, consistent with the Blasius similarity solution. Equations (5.2) and (5.3) make a stronger assumption by neglecting the non-parallel shear terms and wall-normal advection all together.

The next approximation comes from the observation that the most linearly amplified modes have small wall-normal components relative to the spanwise and streamwise components. This is plotted in figure 12 where $\|\psi_{v,1}\|_r$ contributes less than 5% of $\|\psi_1\|_r$. As a result, the contribution from (5.2) is negligible in the numerator of (2.7) and $\|\psi_1\|_r^2 \approx \|\psi_{u,1}\|_r^2 + \|\psi_{w,1}\|_r^2 = \|(\partial_{xx} - k_z^2)\psi_{\omega,1}\|_r^2$, where $\psi_{\omega,1} = ik_z\psi_{u,1} - \partial_x\psi_{w,1}$ (see the Appendix). Because it was assumed that k_z and the streamwise derivatives are $O(1)$, it can be further assumed that $\|\psi_1\|_r^2 \sim \|\psi_{\omega,1}\|_r^2$. By using the approximations that $\psi_{v,1}$ is negligible and that only outer region forcing is optimal, the linear amplification can be approximated as

$$\tilde{\sigma}_1 \approx \max_{\|\hat{f}\|_o=1} \|\hat{\omega}_2\|_o. \tag{5.4}$$

Through application of operator norm inequalities and the triangle inequality using $\|\hat{\omega}_2\|_o$ and (5.3), the approximation $\tilde{\sigma}_1$ is bounded above as

$$\tilde{\sigma}_1 \leq \|\mathcal{L}_{SQ}^{-1}\|_o(\|\hat{f}_\omega\|_o + k_z\|\bar{U}_y\|_o\|\mathcal{L}_{OS}^{-1}\hat{f}_v\|_o). \tag{5.5}$$

Equation (5.5) gives an upper bound to the approximation of $\tilde{\sigma}_1$ based on linear growth with \bar{U}_y . Similarly, if the forcing is constrained to only wall-normal forcing, it must be the case that

$$\max_{\|\hat{f}\|_o=1, \hat{f}_u=\hat{f}_w=0} \|\hat{\omega}_2\|_o \leq \tilde{\sigma}_1. \tag{5.6}$$

In other words, the largest possible gain that stems from solely wall-normal forcing is less than the optimal gain. Equation (5.6) can be written explicitly by setting $\hat{f}_\omega = 0$ in (5.3) to establish the lower bound as

$$k_z\|\mathcal{L}_{SQ}^{-1}\|_o\|\bar{U}_y\|_o\|\mathcal{L}_{OS}^{-1}\hat{f}_v\|_o \leq \tilde{\sigma}_1. \tag{5.7}$$

Together, (5.5) and (5.7) suggest that $\tilde{\sigma}_1$ is bounded below by a quantity that scales with $\|\bar{U}_y\|_o$ and bounded above by a quantity that grows linearly with $\|\bar{U}_y\|_o$.

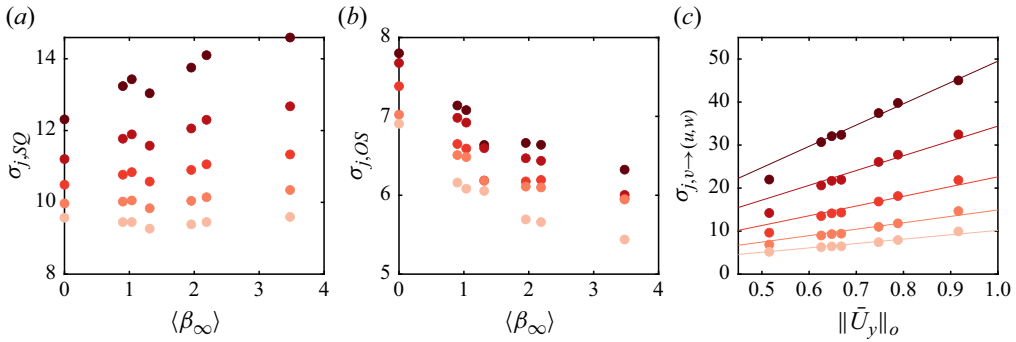


Figure 13. Plots of the first five resolvent gains of \mathcal{L}_{SQ} (a), \mathcal{L}_{OS} (b) and the full operator with componentwise masking to consider only \hat{f}_v forcing and \hat{u} and \hat{w} response (c) for the representative mode from figure 8. Panels (a) and (b) are plotted against $\langle\beta_\infty\rangle$ while (c) is plotted against $\|\bar{U}_y\|_o$. The solid lines in (c) denote lines of best fit for each of the $\sigma_{j,v\rightarrow(u,w)}$. Note that the lighter colours denote increasing j .

It must be noted that the \bar{U}_y dependence in both (5.6) and (5.7) also depends on the amplification from \mathcal{L}_{OS}^{-1} and \mathcal{L}_{SQ}^{-1} , measured in the outer region of the flow. To show that the amplification from \mathcal{L}_{SQ}^{-1} will not produce a significant additional \bar{U} dependence on the upper and lower bounds, its resolvent gains, $\sigma_{j,SQ}$, are plotted in figure 13(a) for the representative mode from figure 8. Recall that $\sigma_{1,SQ} = \|\mathcal{L}_{SQ}^{-1}\| \approx \|\mathcal{L}_{SQ}^{-1}\|_o$. Here $\sigma_{j,SQ}$ has a slight $\langle\beta_\infty\rangle$ dependence for the optimal modes, where $\sigma_{1,SQ}$ grows by 18% between $\langle\beta_\infty\rangle = 0$ to $\langle\beta_\infty\rangle = 3.47$. For reference, σ_1 grows by 187% over the same $\langle\beta_\infty\rangle$ range. For the higher-order modes, the $\sigma_{j,SQ}$ variation with $\langle\beta_\infty\rangle$ is negligible compared with the variation in σ_5 . Furthermore, \mathcal{L}_{SQ}^{-1} is not low-rank as the first five $\sigma_{j,SQ}$ are all within the same order of magnitude. This means that it is more than likely that $(\hat{f}_\omega + ik_z\bar{U}_y\mathcal{L}_{OS}^{-1}\hat{f}_v)$ in (5.3) is composed of higher-order forcing modes of \mathcal{L}_{SQ}^{-1} that have weak \bar{U} dependence. As a result, it can be concluded that the upper bound in (5.5) is weakly dependent on the \bar{U} -dependence on $\|\mathcal{L}_{SQ}^{-1}\|_o$.

To estimate the amplification from \mathcal{L}_{OS}^{-1} , componentwise masking is applied to consider the amplification from \hat{f}_v to \hat{v} so as to only consider the $\mathcal{L}_{OS}^{-1}\hat{f}_v$ term in (5.2). These resolvent gains are denoted as $\sigma_{j,OS}$ and are plotted in figure 13(b). Here $\sigma_{j,OS}$ demonstrates a slight decrease with $\langle\beta_\infty\rangle$ with a decrease of approximately 20% between the $\langle\beta_\infty\rangle$ range. The $\sigma_{j,OS}$ also demonstrate a weak \bar{U} dependence on its leading gains. Although the amplification has contributions from \mathcal{L}_{SQ}^{-1} and \mathcal{L}_{OS}^{-1} , it is expected that the \bar{U} -dependence on the amplification only enters the \bar{U}_y term.

To show that the \bar{U} dependence on \mathcal{L}_{SQ}^{-1} and \mathcal{L}_{OS}^{-1} does not affect the lower bound, figure 13(c) plots $\sigma_{1,v\rightarrow(u,w)}$, the resolvent gains when componentwise masking is applied to consider only forcing from \hat{f}_v to a response with \hat{u} and \hat{w} . This mimics the conditions in (5.7) which captures only amplification from the lift-up mechanism. Here, it is found that despite the $\langle\beta_\infty\rangle$ variation in the amplification of \mathcal{L}_{SQ}^{-1} and \mathcal{L}_{OS}^{-1} , the growth in $\sigma_{1,v\rightarrow(u,w)}$ is linear with $\|\bar{U}_y\|_o$. Fitting a line to $\sigma_{1,v\rightarrow(u,w)}$ as

$$\sigma_{j,v\rightarrow(u,w)} = T_j\|\bar{U}_y\|_o, \tag{5.8}$$

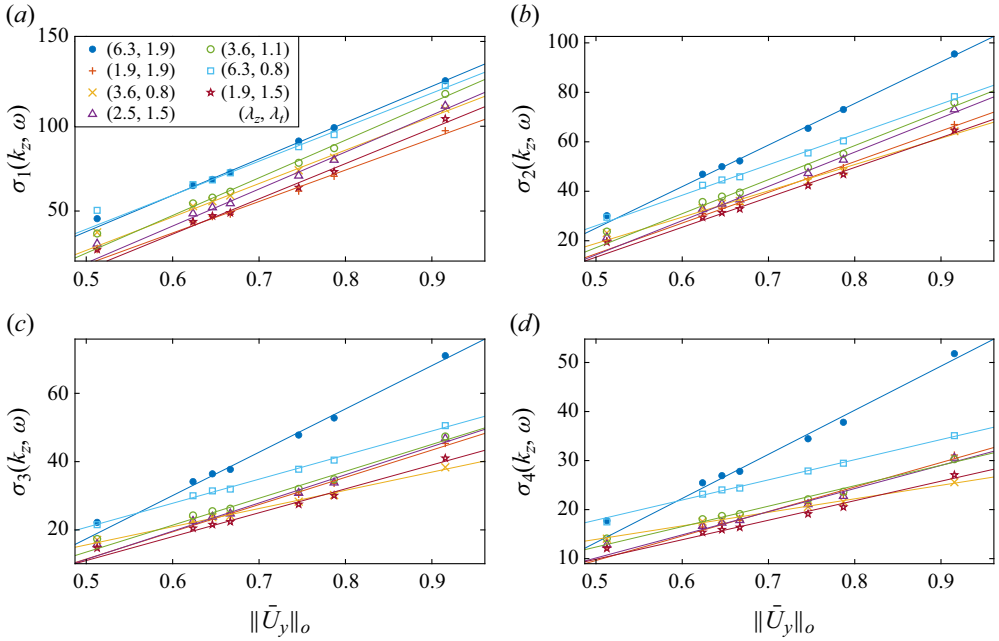


Figure 14. The same as figure 9, except that the σ_j are plotted against $\|\bar{U}_y\|_o$ and the lines of best fit are fitted using $\|\bar{U}_y\|_o$ for the data with $\langle\beta_\infty\rangle$.

where T_j is a constant for each j in figure 13(c), shows that the approximations made in this section can explain the amplification from the lift-up mechanism. Furthermore, it demonstrates that any \bar{U} dependence on \mathcal{L}_{OS}^{-1} and \mathcal{L}_{SQ}^{-1} does not affect the linear growth with $\|\bar{U}_y\|_o$. The differences in the mode shapes are not accounted for in (5.8), which may explain why the lines of best fit do not cross $\sigma_{1,v \rightarrow (u,w)}$ for the ZPG TBL.

The linear fit in (5.8) holds when $\hat{f}_\omega = 0$ such that the assumption in (5.7) holds. For a more general case, a new linear fit is proposed based on the upper bound in (5.5) such that

$$\sigma_j(\lambda_z, \lambda_t) = a_{j,0}(\lambda_z, \lambda_t) + a_{j,1}(\lambda_z, \lambda_t)\|\bar{U}_y\|_o, \tag{5.9}$$

where $a_{j,i}(\lambda_z, \lambda_t)$ are scale-dependent constants for each j . The coefficients $a_{j,0}$ and $a_{j,1}$ are analogous to $\|\mathcal{L}_{SQ}^{-1}\|_o\|\hat{f}_\omega\|_o$ and $k_z\|\mathcal{L}_{SQ}^{-1}\|_o\|\mathcal{L}_{OS}^{-1}\hat{f}_v\|_o$, respectively. These linear fits are shown in figure 14 for the same $\sigma_j(\lambda_z, \lambda_t)$ plotted in figure 9 demonstrating that there is indeed linear growth in σ_j with $\|\bar{U}_y\|_o$ for the APG TBLs as suggested by the upper bound. Furthermore, figure 12(c) shows that the APG TBL datasets used here have mean flow fields such that

$$\|\bar{U}_y\|_o = d_0 + d_1\langle\beta_\infty\rangle, \tag{5.10}$$

where d_0 and d_1 were constants. Taking both (5.9) and (5.10) recovers the linear form in σ_j with $\langle\beta_\infty\rangle$ from (4.1). Hence, it can be concluded that the linear growth of σ_j in $\|\bar{U}_y\|_o$ for the large-scale structures can be predicted from the LNSE if the large-scale modes are supported in the outer region of the flow. Equation (5.9) stems from the dominant terms of the LNSE while the linear fit in (4.1) requires that (5.10) holds, which is not guaranteed for general APG TBLs. Although the linear fit for the APG TBL modes was motivated by neglecting the non-parallel terms by considering $\tilde{\sigma}_1$; σ_1 is significantly larger than $\tilde{\sigma}_1$.

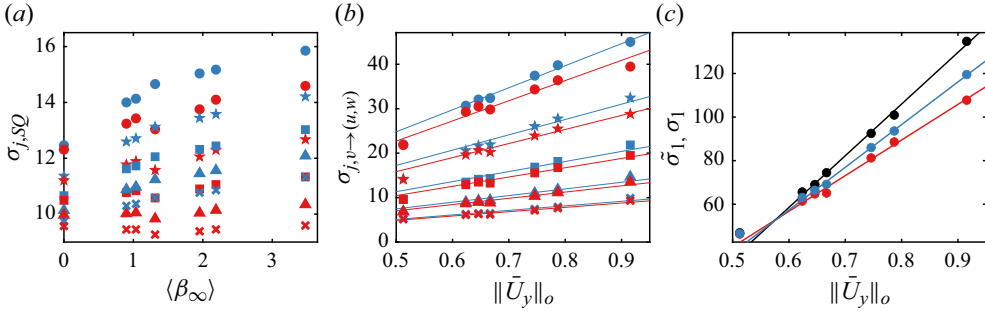


Figure 15. Comparison of $\tilde{\sigma}_{j,SQ}$ (blue) and $\sigma_{j,SQ}$ (red) (a). Here $\sigma_{j,(v \rightarrow u,w)}$ is computed for the full LNSE (blue) and $\tilde{\sigma}_{j,(v \rightarrow u,w)}$ by neglecting \bar{U}_x , \bar{V}_x , and \bar{V} (red) (b). The lines of best fit are fitted using (5.8). Plots of σ_1 (using full LNSE), $\tilde{\sigma}_1$ (neglecting \bar{V} , \bar{V}_x , and \bar{U}_x) and $\bar{\sigma}_1$ (neglecting \bar{V} and \bar{V}_x) in black, red and blue, respectively. The lines of best fit are fitted for $\langle\beta_\infty\rangle > 0$. $j = 1, 2, 3, 4$ and 5 correspond to the circle, star, square, triangle and \times . These are all computed for the representative large-scale mode from figure 8.

This indicates that the non-parallel terms are non-negligible. Next, the influence of the non-parallel terms on the amplification will be examined.

5.2. Influence of the non-parallel terms on the linear amplification

Although artificially neglecting the non-parallel terms in the LNSE can still explain the linear growth with $\langle\beta_\infty\rangle$, figure 11(f) demonstrates that the non-parallel terms are a non-negligible source of amplification. Here, the effect of the non-parallel terms will be examined to discuss their role in the linear amplification. Equations (5.2) and (5.3) are now reconsidered, except that the \mathcal{L}_{SQ} operators are augmented to incorporate the \bar{U}_x terms as $\tilde{\mathcal{L}}_{SQ} = \mathcal{L}_{SQ} + \bar{U}_x$ while the \mathcal{L}_{OS} operators are left unchanged because their amplification was shown to be approximately independent of $\langle\beta_\infty\rangle$ when using the full LNSE in figure 13(b). Incorporating \bar{U}_x also introduces off-diagonal terms in the full OSS, though they are negligible relative to the mean shear, $k_z \|\bar{U}_y\|_o$. Since only \mathcal{L}_{SQ} has changed, an upper and lower bound for σ_1 can be constructed by following the steps in § 5.1 as

$$k_z \|\tilde{\mathcal{L}}_{SQ}^{-1} \bar{U}_y \mathcal{L}_{OS}^{-1} \hat{f}_v\|_o \leq \sigma_1 \leq \|\tilde{\mathcal{L}}_{SQ}^{-1}\|_o (\|\hat{f}_\omega\|_o + k_z \|\bar{U}_y\|_o \|\mathcal{L}_{OS}^{-1} \hat{f}_v\|_o). \quad (5.11)$$

The effect of \bar{U}_x is to augment the amplification of $\tilde{\mathcal{L}}_{SQ}$. This can be seen by computing the resolvent amplification of $\tilde{\mathcal{L}}_{SQ}$, $\tilde{\sigma}_{1,SQ}$ and comparing with the $\sigma_{j,SQ}$ of \mathcal{L}_{SQ} in figure 15(a). It can be seen that $\tilde{\sigma}_{j,SQ} > \sigma_{j,SQ}$ for $j = 1, 2, 3, 4, 5$, indicating that the inclusion of \bar{U}_x increases the amplification by 10%. This increase in amplification then manifests itself as an increase in the amplification via the lift-up effect. To show this, $\sigma_{j,(v \rightarrow u,w)}$ is compared with $\tilde{\sigma}_{j,(v \rightarrow u,w)}$, the resolvent amplification from \hat{f}_v to (\hat{u}, \hat{w}) for the LNSE neglecting \bar{U}_x , \bar{V}_x and \bar{V} , in figure 15(b), demonstrating that $\sigma_{j,(v \rightarrow u,w)} > \tilde{\sigma}_{j,(v \rightarrow u,w)}$. From the lines of best fit, the rate of growth with $\|\bar{U}_y\|_o$ is larger for the full LNSE ($\sigma_{j,(v \rightarrow u,w)}$) than by neglecting the non-parallel terms ($\tilde{\sigma}_{j,(v \rightarrow u,w)}$). From the lower bound in (5.11), the increased rate of growth stems from the increase in amplification of $\tilde{\mathcal{L}}_{SQ}^{-1}$ since it was argued that \mathcal{L}_{OS}^{-1} was hardly affected by the change in base flow. This increased rate of growth with $\|\bar{U}_y\|_o$ then manifests itself as a larger $a_{j,1}$ from (5.9). This can be seen in figure 15(c) where $\bar{\sigma}_1$ is computed for the LNSE where only \bar{V} and \bar{V}_y are

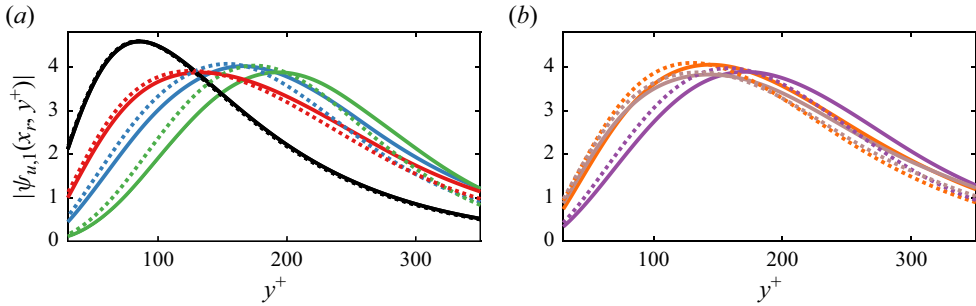


Figure 16. Plots of $|\psi_{1,u}|$ at x_{r2} for the representative large-scale mode. The dotted lines are computed with \bar{V} and \bar{V}_x set to 0 while the solid lines are computed with the full LNSE. Panels (a) and (b) are separated for visibility. The lines are colour coded according to table 1.

neglected. By including \bar{U}_x , $\bar{\sigma}_1 > \tilde{\sigma}_1$. Since \mathcal{L}_{SQ}^{-1} also amplifies \hat{f}_ω , the magnitude of $a_{j,0}$ is also increased when \bar{U}_x is included.

The inclusion of the \bar{V} terms provide wall-normal advection that is neither present in the ZPG TBL, nor in LNSE with artificially neglected \bar{V} . This can be seen in figure 16(a,b), where $|\psi_{1,u}|$ is compared using the full LNSE and the LNSE with \bar{V} and \bar{V}_x artificially set to 0. It can be seen that the modes computed with the full LNSE reach their peak amplitude farther from the wall than the artificial modes. As the APG strength increases, the disparity between the two sets of modes increases, as can be seen by comparing the m13 and b1n modes. As expected, the ZPG modes are almost indistinguishable. Because the modes computed with stronger APG are farther from the wall, they experience a stronger streamwise varying \bar{U} . As a result, the modes computed with the full LNSE experience a stronger convective non-normality and thus increased amplification from the \mathcal{L}_{SQ}^{-1} term. As a result, for σ_1 , both $a_{j,1}$ and $|a_{j,0}|$ are the largest in figure 15(c), indicating a further increase in amplification when none of the non-parallel terms are neglected.

6. Discussion

Biglobal resolvent analysis in a long streamwise domain permits the study of pressure gradient history and the effects of streamwise growth (non-parallel effects) in the APG TBL on linear amplification. Because this analysis derives from the LNSE, it is possible to analytically track how these effects manifest themselves in the linear amplification. Through a scale-based analysis, the linear growth in σ_j with $\langle \beta_\infty \rangle$ follows from the behaviour of the mean flow fields in the near-equilibrium APG TBLs through (5.10) and the role of the componentwise amplification in the upper and lower bounds in (5.5) and (5.7).

Even by including the non-parallel terms, the resolvent amplification was still shown to grow linearly with $\|\bar{U}_y\|_o$, for the APG TBLs rather than the ZPG TBL. This was likely due to the differences in the outer region of the mean flow fields (Wei & Knopp 2023), which in turn changed where the modes are localized in the ZPG case. For the APG TBLs, the mean flow fields did not significantly affect the resolvent mode shape.

Extending the linear growth of σ_j to $\langle \beta_\infty \rangle$ in (4.1) requires that both (4.1) and (5.9) hold. It is expected that (4.1) is more sensitive to the choice of \bar{U} than (5.9) because the former requires that both (5.10) and (5.9) hold. The datasets studied herein were ‘near-equilibrium’ TBL (Bobke *et al.* 2017) at relatively similar Re_τ and similar free

stream boundary conditions such that $U_\infty \sim (x - x_d)^m$ with mild to moderate β . Due to the similarity in the APG TBLs, (4.1) held well for the APG TBL datasets. However, it is expected that for datasets with strong APG, the non-parallel terms may be non-negligible and create sources of amplification that can cause the linear fit with $\|\bar{U}_y\|_o$ to fail. Furthermore, it is expected that APG TBL with non-equilibrium conditions, like strongly varying $\beta(x)$ or flow separation, could make (4.1) not hold since \bar{U} would experience significant non-parallel terms which could cause (5.9) to fail.

While the explanations in § 5 were used to explain why σ_1 grows monotonically with $\langle\beta_\infty\rangle$, they can also be used to explain the secondary peaks of \hat{E}^+ that become more amplified with increasing $\beta(x_{r1})$ present in figure 5. Since the datasets used in figure 5 were characterized by regions with nearly constant values of $\beta(x)$, this discussion will approximate $\langle\beta_\infty\rangle$ as $\beta(x_{r1})$. The integrand of \hat{E}^+ , $|\sigma_1^+ \psi_{u,1}^+|^2$, scales differently for the near-wall small-scale modes and the outer-region large-scale modes. First, due to the choice of normalization, $\sigma_j^+ = Re_\tau^2(x_{r1})Re^{-1}(x_{r1})\sigma_j$ and $\psi_{u,j}^+ = \sqrt{Re_\tau}\psi_{u,j}$. For the small-scale modes, it can be shown that if \bar{U}^+ is self-similar where ψ_1 is supported, then σ_1^+ and $\psi_{u,1}^+$ are also self-similar (Moarref *et al.* 2013; Gomez 2024). In the case of a mild APG TBL at low Re_τ , the log-layer is affected by the APG, which affects the self-similarity of the near-wall modes, especially the higher-order modes (Gomez 2024). However, for the leading modes, these near-wall APG effects were small enough that the near-wall linear amplification of the APG TBL could still resemble that of the ZPG TBL. As a result, the integrand in \hat{E}^+ , $|\sigma_1^+ \psi_{u,1}^+|^2$, is only slightly affected by β . While this study focused on mild to moderate APGs, strong APGs that can cause separation are expected to significantly affect the near-wall amplification.

For the large-scale modes, the small variation in $\|\psi_{u,1}\|_r$ with $\langle\beta_\infty\rangle$ in figure 12(a) allows the approximation that the amplitude of the large-scale modes, $|\psi_{u,1}|$, is independent of $\langle\beta_\infty\rangle$. Although figure 8 showed that the increased \bar{V} in stronger APG TBL advected the $\psi_{u,1}$ farther from the wall, this effect will be neglected for this discussion since it is only focused on the magnitude of the modes rather than their shape. As a result, the amplitudes of the large-scale modes, $|\psi_{u,1}^+|$, are approximated to be independent of $\langle\beta_\infty\rangle$ in the calculation of E^+ . Following (4.1),

$$\sigma_j^+(\lambda_z, \lambda_t) = \frac{Re_\tau^2(x_{r1})}{Re(x_{r1})}\sigma_j(\lambda_z, \lambda_t) \approx \frac{Re_\tau^2(x_{r1})}{Re(x_{r1})}m_{j,0}(\lambda_z, \lambda_t)[1 + m_{j,1}(\lambda_t, \lambda_z)\langle\beta_\infty\rangle]. \quad (6.1)$$

Although $Re(x_{r1})$ increases with $\langle\beta_\infty\rangle$, it is negligible compared with the $1 + m_{j,1}(\lambda_t, \lambda_z)\langle\beta_\infty\rangle$ term such that σ_j^+ increases with $\langle\beta_\infty\rangle$. Thus, the increased amplification of large-scale modes in \hat{E}^+ can be explained solely by the increase in σ_1 with $\langle\beta_\infty\rangle$ for the large-scale modes.

The biglobal resolvent approach is able to qualitatively capture various effects seen in APG TBL. For example, the large-scale energization with increasing β is reflected in the increased large-scale amplification with increasing β along with the near-wall self-similarity of the small-scale structures. Of particular interest is how the history effect is shown to affect both the large-scale linear amplification and the outer region Reynolds stresses (Bobke *et al.* 2017; Tanarro *et al.* 2020). One way in which the monotonic growth with $\langle\beta_\infty\rangle$ enters the outer region turbulent fluctuations is through the linear growth in σ_j with $\langle\beta_\infty\rangle$. This means that the linear amplification of large-scale nonlinear interactions by the APG mean flow fields increases with $\langle\beta_\infty\rangle$, which may be reflected in the large-scale turbulent fluctuations. The collapse of the Reynolds stresses with u_{hyb}^2 , which is linear in

$\langle \beta_\infty \rangle$, may point to a connection between the linear amplification studied herein and the true nonlinear nature of the APG TBLs.

7. Conclusion

A biglobal resolvent approach was used to study spatially developing TBL flows over flat plates and identify the relative influences of non-parallel componentwise non-normalities from \bar{V}_x , convective non-normalities, wall-normal advection and the pressure gradient history effect on linear amplification in near-equilibrium mild to moderate APG TBL (Bobke *et al.* 2017; Pozuelo *et al.* 2022) and high Re_τ ZPG TBL (Eitel-Amor *et al.* 2014). The effects of Re_τ , β and $\langle \beta_\infty \rangle$ on the analysis were investigated.

Applying a spatial mask to measure the response amplification in the vicinity of x_r allowed both small-scale and large-scale modes to have a non-zero response at x_r . This allowed for the study of local β effects at fixed Re_τ and local Re_τ effects on the linear amplification. Furthermore, the premultiplied amplification, $\hat{E}(y, k_z)$, is used as a rank-one approximation of the premultiplied energy spectra for a velocity fluctuation defined as $\hat{u} = \sigma_1 \psi_{u,1}$. Although it does not have any nonlinear closure, \hat{E} was shown to reflect certain characteristics seen in the premultiplied energy spectra in simulations. One feature is the presence of a near-wall peak using both the ZPG and APG TBL base flows. The inner peak was shown to be self-similar for \bar{U} with near-wall self-similarity such as the ZPG TBL datasets and the high Re_τ APG TBL of Pozuelo *et al.* (2022). A secondary outer peak for large λ_z is also present for the linear amplification of the low Re_τ APG TBLs of Bobke *et al.* (2017) and is notably absent in the low Re_τ ZPG TBL. For this secondary peak, \hat{E}^+ was shown to increase with $\beta(x_{r1})$. Similarly, for the ZPG TBL, \hat{E}^+ was shown to increase with Re_τ for the large λ_z away from the wall and demonstrate evidence of a secondary peak for the largest Re_τ interrogated.

By applying a spatial mask to consider only the region upstream of x_{r2} in the inner products, the biglobal resolvent analysis was used to investigate how the linear amplification varies due to the upstream history. This history is measured through $\langle \beta_\infty \rangle$, the upstream average of β_∞ over the same computational domain. It was found that the σ_j increased linearly with $\langle \beta_\infty \rangle$. By drawing similarities to the linear variation in β in the hybrid velocity scale of Romero *et al.* (2022) and Sekimoto *et al.* (2019), an augmented hybrid velocity scale, u_{hyb} was posed that incorporates a measure of the history effect through a linear dependence with $\langle \beta_\infty \rangle$. Rescaling the Reynolds stresses with u_{hyb}^2 mitigated the APG-related outer peaks and improved the collapse of the Reynolds stresses compared with u_h . This linked the monotonic growth in the secondary outer peaks of \overline{uu}^+ with $\langle \beta_\infty \rangle$ with the linear growth of σ_j with $\langle \beta_\infty \rangle$.

Finally, an explanation based on the lift-up mechanism is offered to explain the increase in σ_1 . It was shown that neglecting the \bar{U}_x , \bar{V}_x and \bar{V} terms in the LNSE still allowed for linear growth with $\langle \beta_\infty \rangle$, albeit with reduced amplification than the full system. As a result, a simplified two-dimensional OSS system was constructed. By using the triangle inequality, it was shown that for this simplified system, σ_1 was bounded below and above by terms that grew linearly with $\|\bar{U}_y\|_o$, a measure of the mean shear in the outer region of the flow. Thus, the equations suggest the σ_1 grows linearly with $\|\bar{U}_y\|_o$. Furthermore, it was shown that for these datasets, $\|\bar{U}_y\|_o$ also grows linearly with $\langle \beta_\infty \rangle$. As a result, σ_1 was shown to grow linearly with $\langle \beta_\infty \rangle$ for the APG TBL flows from an analysis of the LNSE and a property of the datasets used herein. It was also shown that the non-parallel terms add additional amplification by increasing the role of the convective non-normality.

The inclusion of the non-parallel shear terms only affected the linear fit with $\|\bar{U}_y\|_o$ by increasing the magnitude of the linear fit's coefficients.

The key result of the study is that several features associated with APG TBLs can be identified through study of the linear operator by consideration of the optimal amplification, i.e. using a rank-one approximations. Changes in free stream \bar{U} and streamwise pressure gradient \bar{P} are encoded in the mean fields and thus change the amplification associated with the resolvent operator. It is encouraging for modellers that these effects can be identified without detailed knowledge of the nonlinear forcing, which would require a large amount of data to cover the range of APGs investigated here. However, any resolvent reconstruction will require nonlinear closure through scale-dependent coefficients and higher-order modes, as is well known for the ZPG and other flow cases.

Most of this study focused on APG TBL in regimes that can be described as near-equilibrium and at lower Re_τ , in accordance with the data available in the literature. Extending these results to high Re_τ APG TBL would require an APG TBL database over a large streamwise domain. Future studies will be used to investigate APG TBL where the β variation is more severe or where separation is approached.

Acknowledgements. We gratefully acknowledge S. Romero and J. Klewicki for discussions regarding the hybrid velocity scaling, and R. Vinuesa for sharing the TBL database.

Funding. This work is supported by the U.S. Office of Naval Research through grants N00014-17-1-2307 and N00014-17-1-3022.

Declaration of interests. The authors report no conflict of interest.

Author ORCIDs.

 Salvador R. Gomez <https://orcid.org/0000-0002-7568-721X>;

 Beverley J. McKeon <https://orcid.org/0000-0003-4220-1583>.

Appendix. Simplified biglobal Orr–Sommerfeld operator

For brevity, the sponge layer terms are ignored with their effect only used to enforce compactness in the forcing and response modes. It is noted that the optimal forcing modes are solenoidal vectors (Rosenberg 2018) such that

$$\nabla^2 \hat{p} = -2 \frac{\partial \bar{U}_i}{\partial x_j} \frac{\partial \hat{u}_j}{\partial x_i}. \tag{A1}$$

The wall-parallel velocities can be written in terms of $\hat{\omega}_2$ and \hat{v} as

$$\hat{u} = (\partial_{xx} - k_z^2)^{-1} \left(ik_z \hat{\omega}_2 - \frac{\partial \hat{v}}{\partial x} y \right), \tag{A2}$$

$$\hat{w} = (\partial_{xx} - k_z^2)^{-1} \left(-\frac{\partial \hat{\omega}_2}{\partial x} - ik_z \frac{\partial \hat{v}}{\partial y} \right). \tag{A3}$$

Assuming compact support in $\hat{\omega}_2$ and \hat{v} , in turn making $(\partial_{xx} - k_z^2)^{-1}$ self-adjoint, the kinetic energy is then

$$\|\hat{u}\|^2 = \frac{1}{L_x} \int \int \left((\partial_{xx} - k_z^2)^{-1} \left[\hat{\omega}_2^* \hat{\omega}_2 + \frac{\partial \hat{v}^*}{\partial y} \frac{\partial \hat{v}}{\partial y} \right] + \hat{v}^* \hat{v} \right) dx dy. \tag{A4}$$

An equation for \hat{v} can be written by substituting (A1) for \hat{p} in the wall-normal component of the LNSE as

$$\begin{aligned} & \left(-i\omega + \bar{U} \cdot \nabla - \frac{\partial \bar{U}}{\partial x} - \frac{1}{Re} \nabla^2 \right) \hat{v} - 2\nabla^{-2} \frac{\partial}{\partial y} \left(\frac{\partial \bar{U}}{\partial y} \frac{\partial \hat{v}}{\partial x} - \frac{\partial \bar{U}}{\partial x} \frac{\partial \hat{v}}{\partial y} \right) \\ & + 2\nabla^{-2} (\partial_{xx} - k_z^2)^{-1} \frac{\partial}{\partial y} \left(\frac{\partial \bar{U}}{\partial x} \frac{\partial^3 \hat{v}}{\partial x^2 \partial y} \right) - 2ik_z \nabla^{-2} (\partial_{xx} - k_z^2)^{-1} \frac{\partial}{\partial y} \left(\frac{\partial \bar{U}}{\partial x} \frac{\partial \hat{\omega}_2}{\partial x} \right) \\ & + \left(\frac{\partial \bar{V}}{\partial x} \hat{u} \right) - 2\nabla^{-2} \frac{\partial}{\partial y} \left(\frac{\partial \bar{V}}{\partial x} \frac{\partial \hat{u}}{\partial y} \right) = \hat{f}_v. \end{aligned} \tag{A5}$$

The terms proportional to \bar{V}_x are not expanded since they will be neglected later. Similarly, by taking the wall-normal component of the curl of the LNSE, an equation for $\hat{\omega}_2$ can be written as follows:

$$\begin{aligned} & \left(-i\omega + \bar{U} \cdot \nabla + \frac{\partial \bar{U}}{\partial x} - \frac{1}{Re} \nabla^2 \right) \hat{\omega}_2 + \frac{\partial \bar{V}}{\partial x} (\partial_{xx} - k_z^2)^{-1} \frac{\partial \hat{\omega}_2}{\partial x} y \\ & + ik_z \left(\frac{\partial \bar{U}}{\partial y} \hat{v} + \frac{\partial \bar{V}}{\partial x} (\partial_{xx} - k_z^2)^{-1} \frac{\partial^2 \hat{v}}{\partial y^2} \right) = \hat{f}_2. \end{aligned} \tag{A6}$$

By using the observation that $|\bar{V}_x| \ll |\bar{U}_x|$, (A5) and (A6) can be written as

$$\mathcal{A}_{OS} \hat{v} + \mathcal{P}_s \hat{\omega}_2 = \hat{f}_v, \tag{A7}$$

$$\mathcal{M}_s \hat{v} + \mathcal{A}_{SQ} \hat{\omega}_2 = \hat{f}_2. \tag{A8}$$

This linear system can be solved for explicitly as

$$\left. \begin{aligned} \hat{v} &= [\mathcal{A}_{OS}^{-1} - \mathcal{A}_{OS}^{-1} \mathcal{P}_s (\mathcal{M}_s^{-1} \mathcal{A}_{SQ} - \mathcal{A}_{OS}^{-1} \mathcal{P}_s)^{-1} \mathcal{A}_{OS}^{-1} \hat{f}_v] \\ &+ \mathcal{A}_{OS}^{-1} \mathcal{P}_s (\mathcal{M}_s^{-1} \mathcal{A} - \mathcal{A}_{OS}^{-1} \mathcal{P}_s)^{-1} \mathcal{M}_s^{-1} \hat{f}_2 \\ \hat{\omega}_2 &= (\mathcal{M}_s^{-1} \mathcal{A}_{SQ} - \mathcal{A}_{OS}^{-1} \mathcal{P}_s)^{-1} (\mathcal{A}_{OS}^{-1} \hat{f}_v - \mathcal{M}_s^{-1} \hat{f}_2) \end{aligned} \right\}. \tag{A9}$$

Together, (A9) forms the OSS system, with \bar{V}_x neglected. Due to the \mathcal{P}_s term, there is an off-diagonal entry that introduces componentwise non-normality into the OSS system by allowing forcing from \hat{f}_2 to \hat{v} caused by \bar{U}_x . However, for the APG TBL studied in this section, the presence of \mathcal{P}_s does not cause $\|\psi_{1,v}\|$ to increase as the APG strength increases. This is likely because the off-diagonal component related to the mean shear scales with \bar{U}_y , while the other off-diagonal term scales with \bar{U}_x . Due to this, the $\mathcal{A}_{OS}^{-1} \mathcal{P}_s (\mathcal{M}_s^{-1} \mathcal{A} - \mathcal{A}_{OS}^{-1} \mathcal{P}_s)^{-1} \mathcal{M}_s^{-1}$ term will be neglected. Next, it is noted that $\mathcal{M}_s^{-1} \mathcal{A}_{SQ} \sim O(\delta_{99})$ while $\mathcal{A}_{OS}^{-1} \mathcal{P}_s \sim O(\delta_{99} U_\infty \partial U_\infty / \partial x)$. As a result, the $\mathcal{A}_{OS}^{-1} \mathcal{P}_s$ term can be neglected such that the following simplified OSS can be established:

$$\left. \begin{aligned} \hat{v} &= \mathcal{A}_{OS}^{-1} \hat{f}_v \\ \hat{\omega}_2 &= \mathcal{A}_{SQ}^{-1} (\mathcal{M}_s \mathcal{A}_{OS}^{-1} \hat{f}_v - \hat{f}_2) \end{aligned} \right\}. \tag{A10}$$

Finally, by neglecting the \bar{U}_x and \bar{V} terms, the simplified OSS system in (5.2) and (5.7) can be recovered. For clarity,

$$\begin{aligned} \mathcal{A}_{OS}\hat{v} = & \left(-i\omega + \bar{U} \cdot \nabla - \frac{\partial \bar{U}}{\partial x} - \frac{1}{Re} \nabla^2 \right) \hat{v} - 2\nabla^{-2} \frac{\partial}{\partial y} \left(\frac{\partial \bar{U}}{\partial y} \frac{\partial \hat{v}}{\partial x} - \frac{\partial \bar{U}}{\partial x} \frac{\partial \hat{v}}{\partial y} \right) \\ & + 2\nabla^{-2} (\partial_{xx} - k_z^2)^{-1} \frac{\partial}{\partial y} \left(\frac{\partial \bar{U}}{\partial x} \frac{\partial^3 \hat{v}}{\partial x^2 \partial y} \right), \end{aligned} \quad (\text{A11})$$

$$\tilde{\mathcal{L}}_{OS}\hat{v} = \mathcal{A}_{OS}\hat{v} - \bar{V} \frac{\partial \hat{v}}{\partial y} \quad (\text{A12})$$

and

$$\mathcal{L}_{OS}\hat{v} = \left(-i\omega + \bar{U} \partial_x - \frac{1}{Re} \nabla^2 \right) \hat{v} - 2\nabla^{-2} \frac{\partial}{\partial y} \left(\frac{\partial \bar{U}}{\partial y} \frac{\partial \hat{v}}{\partial x} \right). \quad (\text{A13})$$

REFERENCES

- ABREU, L.I., CAVALIERI, A.V.G., SCHLATTER, P., VINUESA, R. & HENNINGSON, D.S. 2020 Spectral proper orthogonal decomposition and resolvent analysis of near-wall coherent structures in turbulent pipe flows. *J. Fluid Mech.* **900**, A11.
- ABREU, L.I., TANARRO, A., CAVALIERI, A.V.G., SCHLATTER, P., VINUESA, R., HANIFI, A. & HENNINGSON, D.S. 2021 Spanwise-coherent hydrodynamic waves around flat plates and airfoils. *J. Fluid Mech.* **927**, A1.
- AUBERTINE, C.D. & EATON, J.K. 2005 Turbulence development in a non-equilibrium turbulent boundary layer with mild adverse pressure gradient. *J. Fluid Mech.* **532**, 345–364.
- BAIDYA, R., PHILIP, J., HUTCHINS, N., MONTY, J.P. & MARUSIC, I. 2017 Distance-from-the-wall scaling of turbulent motions in wall-bounded flows. *Phys. Fluids* **29** (2), 020712.
- BOBKE, A., VINUESA, R., ÖRLÜ, R. & SCHLATTER, P. 2017 History effects and near equilibrium in adverse-pressure-gradient turbulent boundary layers. *J. Fluid Mech.* **820**, 667–692.
- CHEVALIER, M., SCHLATTER, P., LUNDBLADH, A. & HENNINGSON, D.S. 2007 SIMSON: a pseudo-spectral solver for incompressible boundary layer flows. TRITA-MEK 2007:07. KTH Mechanics, Stockholm.
- CHOMAZ, J.-M. 2005 Global instabilities in spatially developing flows: non-normality and nonlinearity. *Annu. Rev. Fluid Mech.* **37**, 357–392.
- CLAUSER, F.H. 1954 Turbulent boundary layers in adverse pressure gradients. *J. Aeronaut. Sci.* **21** (2), 91–108.
- COLES, D. 1956 The law of the wake in the turbulent boundary layer. *J. Fluid Mech.* **1** (2), 191–226.
- COSSU, C., PUJALS, G. & DEPARDON, S. 2009 Optimal transient growth and very large-scale structures in turbulent boundary layers. *J. Fluid Mech.* **619**, 79–94.
- DAVIS, T.B., UZUN, A. & ALVI, F.S. 2019 Optimal disturbances and large-scale energetic motions in turbulent boundary layers. *J. Fluid Mech.* **860**, 40–80.
- DEL ALAMO, J.C. & JIMENEZ, J. 2006 Linear energy amplification in turbulent channels. *J. Fluid Mech.* **559**, 205–213.
- DESPANDE, R., VAN DEN BOGAARD, A., VINUESA, R., LINDIĆ, L. & MARUSIC, I. 2023 Reynolds-number effects on the outer region of adverse-pressure-gradient turbulent boundary layers. *Phys. Rev. Fluids* **8** (12), 124604.
- EITEL-AMOR, G., ÖRLÜ, R. & SCHLATTER, P. 2014 Simulation and validation of a spatially evolving turbulent boundary layer up to $re_\theta = 8300$. *Intl J. Heat Fluid Flow* **47**, 57–69.
- GOMEZ, S.R. 2024 Linear amplification in nonequilibrium turbulent boundary layers. PhD thesis, California Institute of Technology.
- GUNGOR, A.G., MACIEL, Y., SIMENS, M.P. & SORIA, J. 2016 Scaling and statistics of large-defect adverse pressure gradient turbulent boundary layers. *Intl J. Heat Fluid Flow* **59**, 109–124.
- HARUN, Z., MONTY, J.P., MATHIS, R. & MARUSIC, I. 2013 Pressure gradient effects on the large-scale structure of turbulent boundary layers. *J. Fluid Mech.* **715**, 477–498.
- HOYAS, S. & JIMÉNEZ, J. 2006 Scaling of the velocity fluctuations in turbulent channels up to $re\tau = 2003$. *Phys. Fluids* **18** (1), 011702.

- HUTCHINS, N., NICKELS, T.B., MARUSIC, I. & CHONG, M.S. 2009 Hot-wire spatial resolution issues in wall-bounded turbulence. *J. Fluid Mech.* **635**, 103–136.
- HWANG, Y. & COSSU, C. 2010 Linear non-normal energy amplification of harmonic and stochastic forcing in the turbulent channel flow. *J. Fluid Mech.* **664**, 51–73.
- JEUN, J., NICHOLS, J.W. & JOVANOVIĆ, M.R. 2016 Input-output analysis of high-speed axisymmetric isothermal jet noise. *Phys. Fluids* **28** (4), 047101.
- JOVANOVIĆ, M.R. & BAMIEH, B. 2005 Componentwise energy amplification in channel flows. *J. Fluid Mech.* **534**, 145–183.
- KAMAL, O., RIGAS, G., LAKEBRINK, M.T. & COLONIUS, T. 2020 Application of the one-way Navier–Stokes (owns) equations to hypersonic boundary layers. In *AIAA Aviation 2020 Forum*, p. 2986. AIAA.
- KITSIOS, V., ATKINSON, C., SILLERO, J.A., BORRELL, G., GUNGOR, A.G., JIMÉNEZ, J. & SORIA, J. 2016 Direct numerical simulation of a self-similar adverse pressure gradient turbulent boundary layer. *Intl J. Heat Fluid Flow* **61**, 129–136.
- LEE, J.H. 2017 Large-scale motions in turbulent boundary layers subjected to adverse pressure gradients. *J. Fluid Mech.* **810**, 323–361.
- LEE, M. & MOSER, R.D. 2015 Direct numerical simulation of turbulent channel flow up to $re_\tau \approx 5200$. *J. Fluid Mech.* **774**, 395–415.
- MALIK, M.R. 1990 Numerical methods for hypersonic boundary layer stability. *J. Comput. Phys.* **86** (2), 376–413.
- MARUSIC, I., MATHIS, R. & HUTCHINS, N. 2010 High Reynolds number effects in wall turbulence. *Intl J. Heat Fluid Flow* **31** (3), 418–428.
- MARUSIC, I., MONTY, J.P., HULTMARK, M. & SMITS, A.J. 2013 On the logarithmic region in wall turbulence. *J. Fluid Mech.* **716**, R3.
- MARUSIC, I. & PERRY, A.E. 1995 A wall-wake model for the turbulence structure of boundary layers. Part 2. Further experimental support. *J. Fluid Mech.* **298**, 389–407.
- MATTSSON, K. & NORDSTRÖM, J. 2004 Summation by parts operators for finite difference approximations of second derivatives. *J. Comput. Phys.* **199** (2), 503–540.
- MCKEON, B.J. & SHARMA, A.S. 2010 A critical-layer framework for turbulent pipe flow. *J. Fluid Mech.* **658**, 336–382.
- MELLOR, G.L. & GIBSON, D.M. 1966 Equilibrium turbulent boundary layers. *J. Fluid Mech.* **24** (2), 225–253.
- MOARREF, R., SHARMA, A.S., TROPP, J.A. & MCKEON, B.J. 2013 Model-based scaling of the streamwise energy density in high-Reynolds-number turbulent channels. *J. Fluid Mech.* **734**, 275–316.
- MONTY, J.P., HARUN, Z. & MARUSIC, I. 2011 A parametric study of adverse pressure gradient turbulent boundary layers. *Intl J. Heat Fluid Flow* **32** (3), 575–585.
- MORRA, P., NOGUEIRA, P.A.S., CAVALIERI, A.V.G. & HENNINGSON, D.S. 2021 The colour of forcing statistics in resolvent analyses of turbulent channel flows. *J. Fluid Mech.* **907**, A24.
- PICKERING, E., RIGAS, G., SCHMIDT, O.T., SIPP, D. & COLONIUS, T. 2021 Optimal eddy viscosity for resolvent-based models of coherent structures in turbulent jets. *J. Fluid Mech.* **917**, A29.
- POPE, S.B. 2000 *Turbulent Flows*. Cambridge University Press.
- POZUELO, R., LI, Q., SCHLATTER, P. & VINUESA, R. 2022 An adverse-pressure-gradient turbulent boundary layer with nearly constant $\beta \simeq 1.4$ up to $re_\theta \simeq 8700$. *J. Fluid Mech.* **939**, A34.
- RAN, W., ZARE, A., HACK, M.J.P. & JOVANOVIĆ, M.R. 2019 Stochastic receptivity analysis of boundary layer flow. *Phys. Rev. Fluids* **4** (9), 093901.
- ROMERO, S.K., ZIMMERMAN, S.J., PHILIP, J. & KLEWICKI, J.C. 2022 Stress equation based scaling framework for adverse pressure gradient turbulent boundary layers. *Intl J. Heat Fluid Flow* **93**, 108885.
- ROSENBERG, K.T. 2018 Resolvent-based modeling of flows in a channel. PhD thesis, California Institute of Technology.
- SAAD, Y. 2011 *Numerical Methods for Large Eigenvalue Problems*, Revised edn. SIAM.
- SANMIGUEL VILA, C., VINUESA, R., DISCETTI, S., IANIRO, A., SCHLATTER, P. & ÖRLÜ, R. 2020 Separating adverse-pressure-gradient and Reynolds-number effects in turbulent boundary layers. *Phys. Rev. Fluids* **5** (6), 064609.
- SCHENK, O. & GÄRTNER, K. 2004 Solving unsymmetric sparse systems of linear equations with pardiso. *Future Gener. Comput. Syst.* **20** (3), 475–487.
- SCHLATTER, P. & ÖRLÜ, R. 2010 Assessment of direct numerical simulation data of turbulent boundary layers. *J. Fluid Mech.* **659**, 116–126.
- SCHMID, P.J. & HENNINGSON, D.S. 2002 *Stability and Transition in Shear Flows*, Applied Mathematical Sciences, vol. 142. Springer Science & Business Media.

Linear analysis characterizes pressure

- SCHMIDT, O.T., TOWNE, A., RIGAS, G., COLONIUS, T. & BRÈS, G.A. 2018 Spectral analysis of jet turbulence. *J. Fluid Mech.* **855**, 953–982.
- SEKIMOTO, A., KITSIOS, V., ATKINSON, C. & SORIA, J. 2019 Outer scaling of self-similar adverse-pressure-gradient turbulent boundary layers. Preprint, [arXiv:1912.05143](https://arxiv.org/abs/1912.05143).
- SIPP, D. & MARQUET, O. 2013 Characterization of noise amplifiers with global singular modes: the case of the leading-edge flat-plate boundary layer. *Theor. Comput. Fluid Dyn.* **27**, 617–635.
- SMITS, A.J., MCKEON, B.J. & MARUSIC, I. 2011 High-Reynolds number wall turbulence. *Annu. Rev. Fluid Mech.* **43**, 353–375.
- SYMON, S., ROSENBERG, K.T., DAWSON, S.T.M. & MCKEON, B.J. 2018 Non-normality and classification of amplification mechanisms in stability and resolvent analysis. *Phys. Rev. Fluids* **3** (5), 053902.
- TANARRO, Á., VINUESA, R. & SCHLATTER, P. 2020 Effect of adverse pressure gradients on turbulent wing boundary layers. *J. Fluid Mech.* **883**, A8.
- TOWNE, A., SCHMIDT, O.T. & COLONIUS, T. 2018 Spectral proper orthogonal decomposition and its relationship to dynamic mode decomposition and resolvent analysis. *J. Fluid Mech.* **847**, 821–867.
- TOWNSEND, A.A.R. 1976 *The Structure of Turbulent Shear Flow*. Cambridge University Press.
- TREFETHEN, L.N. 1999 *Spectra and Pseudospectra: The Behaviour of Non-Normal Matrices and Operators*. Springer.
- VINUESA, R., ÖRLÜ, R., SANMIGUEL VILA, C., IANIRO, A., DISCETTI, S. & SCHLATTER, P. 2017 Revisiting history effects in adverse-pressure-gradient turbulent boundary layers. *Flow Turbul. Combust.* **99**, 565–587.
- VISHWANATHAN, V., FRITSCH, D., LOWE, T.K. & DEVENPORT, W.J. 2021 Analysis of coherent structures over a smooth wall turbulent boundary layer in pressure gradient using spectral proper orthogonal decomposition. In *AIAA Aviation 2021 Forum*, p. 2893. AIAA.
- VOLINO, R.J. 2020 Non-equilibrium development in turbulent boundary layers with changing pressure gradients. *J. Fluid Mech.* **897**, A2.
- WEI, T., FIFE, P., KLEWICKI, J.C. & MCMURTRY, P. 2005 Properties of the mean momentum balance in turbulent boundary layer, pipe and channel flows. *J. Fluid Mech.* **522**, 303–327.
- WEI, T. & KNOPP, T. 2023 Outer scaling of the mean momentum equation for turbulent boundary layers under adverse pressure gradient. *J. Fluid Mech.* **958**, A9.